Bayesian Calibration and Uncertainty Quantification of a Rate-dependent Cohesive Zone Model for Polymer Interfaces

Ponkrshnan Thiagarajan [ID][a], Trisha Sain[b,*], Susanta Ghosh [ID][b,**]

[a]*Department of Civil and Systems Engineering, Johns Hopkins University, MD, USA*
[b]*Department of Mechanical Engineering-Engineering Mechanics, Michigan Technological University, MI, USA*

Abstract

This study presents a rate-dependent cohesive zone model for the fracture of polymeric interfaces and performs a Bayesian calibration, an uncertainty quantification, and a sensitivity analysis for the model. The proposed cohesive zone model accounts for both reversible elastic and irreversible rate-dependent separation sliding deformation at the interface. The viscous dissipation due to the irreversible opening at the interface is modeled using elastic-viscoplastic kinematics that incorporates the effects of strain rate. Inverse calibration of parameters for such complex models through trial and error is challenging due to the large number of parameters of the model. Moreover, the calibrated parameter values are often non-unique and uncertain when the available experimental data is limited. To tackle this challenge, we employ a Bayesian calibration approach to identify parameters from experimental data, the resulting parameters significantly enhance the accuracy of the model. To quantify the uncertainty associated with the inverse parameter estimation, a modular Bayesian approach is employed to calibrate the unknown model parameters, accounting for the parameter uncertainty of the cohesive zone model. The advantages of the Bayesian calibration over a deterministic parameter fit are demonstrated. Further, to quantify the model uncertainties, such as incorrect assumptions or missing physics, a discrepancy function is introduced, which significantly improves the model's prediction. Finally, the total uncertainty of the model is quantified in a predictive setting. A sensitivity analysis is performed to assess how changes

---

*Corresponding author, email:tsain@mtu.edu
**Corresponding author, email:susantag@mtu.edu

in the input variables of the model affect the peak load, facilitating the identification of a concise set of highly influential parameters. The present approach can be used for calibration and uncertainty quantification for other complex computational mechanics models. It should also facilitate the designing of interface materials under uncertainty.

Keywords: Cohesive zone, rate-dependent fracture, viscoplasticity, Bayesian calibration, Uncertainty quantification, Sensitivity analysis

Math symbols and their definitions

Symbol	Definition
Ω^+, Ω^-	Top and bottom bodies of polymeric materials
Γ_{o-}, Γ_{o+}	Lower and upper surfaces of interface
$\mathbf{X}_i$	Cartesian material coordinates
$\mathbf{X}, \mathbf{x}$	Material point in the reference and current configuration
$\mathbf{u}$	Displacement field
t, T	Time
$\boldsymbol{\chi}$	Invertible deformation map
$\mathbf{F}$	Deformation gradient tensor
$\mathbf{N}$, $\mathbf{n}$	Unit normal in reference and current configuration
$\boldsymbol{\delta}$, $\boldsymbol{\delta}^e$, $\boldsymbol{\delta}^p$	Total, elastic and plastic displacement jump across the cohesive interface
ϕ	Free energy per unit surface area in the reference configuration
κ	Hardening variable
D	Scalar damage variable
$\boldsymbol{t}$, $\boldsymbol{t}_N$, $\boldsymbol{t}_T$	Traction vector and its normal and tangential components
H	Hardening modulus
$\boldsymbol{K}$	Interface elastic stiffness tensor
K_N, K_T	Normal and tangential elastic stiffness moduli
t_N	Magnitude of normal stress at the interface

τ	Effective tangential traction
$\boldsymbol{\delta}_N, \boldsymbol{\delta}_T$	Normal and tangential cohesive opening
S_{yp}	Current yield strength
μ	Friction coefficient
S_0	Initial yield stress
γ_{vp}	Viscoplastic strain rate parameter
$\boldsymbol{m}_{flow}$	Plastic flow direction
γ_0	Reference plastic strain parameter
Q	Activation energy
m	Rate sensitivity parameter
k	Boltzmann constant
θ	Reference temperature
δ^0, δ^f	Effective displacement jump at the onset of damage and final failure of the interface
Δ	Crack opening displacement
L, B, h	Interface length, specimen width and height
a_o	Crack length
$\mathbb{X}$	Input to the computational model
$\boldsymbol{Y}$	Quantity of interest
$\boldsymbol{\Theta}$	Calibration parameters
$\boldsymbol{Y}^{(e)}$	Experimental response
$\boldsymbol{Y}^{(c)}$	Computational model response
$\boldsymbol{\delta}_{disc}$	Discrepancy function
$\boldsymbol{\epsilon}$	Measurement error
$\boldsymbol{\Sigma}$	Covariance matrix
$p(\boldsymbol{\Theta})$	Prior distribution of parameters
$p(\boldsymbol{d}|\boldsymbol{\Theta})$	Likelihood of observing the data
$p(\boldsymbol{d})$	Model evidence
$\boldsymbol{d}$	Set of experimental observations

n	Number of experimental observations
N	Gaussian distribution
N_{out}	Number of output dimensions
y_e, y_p	Experimental response and computational model prediction
σ^2	Variance of measurement error

Table 1: Nomenclature of symbols used in the manuscript. Symbols are presented in the order of their appearance.

1. Introduction

Interfaces play a major role in dictating the overall mechanical performance of various composite structures and bi-material joints. Typical demonstration of interface failure includes delamination in laminated composite systems [1], failure of concrete dam-foundation joints [2], debonding of thin films from substrates [3] etc. Such failures occur due to the local stress concentrations leading to separations and tangential sliding of the contacting surfaces across the interface. In the case of adhesively bonded components, the fact that the viscous or rate-dependent properties of the adhesives influence the global fracture response has been well documented in the recent literature [4, 5, 6, 7]. In such cases, the interfacial degradation depends on the rate of applied loading and the final response turns out to be rate-dependent as well.

In the case of polymer composite materials, crack initiation and propagation along the interfaces have been shown to be rate dependent [8, 9, 10]. It has been suggested that the bulk polymer viscous properties in general influence the global fracture response for the composites [11]. To incorporate this rate-dependent behavior in the domain of computational modeling, various phenomenological cohesive laws have been proposed [12, 13, 14]. Earlier work by [15] proposed a rate-dependent crack propagation model for craze-like fracture in polymers and failure of a joint bonded with a thin adhesive layer. In [16], rate-dependent traction-separation relations were developed to simulate the stick-slip fracture in an adhesively bonded aluminum double-cantilever beam (DCB) specimen. In another work, a

4

rate-dependent interface model was formulated considering a viscoplastic framework with hardening/softening behavior for shear and tensile traction [13]. In [17] , a new approach for modeling cracks is proposed based on the cracking particle method. A dynamic cohesive law is proposed that takes into account the change of fracture energy which is then combined with a rate-dependent damage plasticity model. Multiple examples of dynamic fractures are demonstrated. Motivated by the experimentally observed differences in the nature of the propagating crack surfaces depending on the test speed, a nonlinear viscoelastic Kelvin model was introduced to simulate the rate-dependent cohesive response between rubber and steel at different rates under mixed mode loading condition [12]. The rate dependence in both the bulk material and the interface was also considered in a similar model proposed by [18]. In [14] a bilinear traction-separation relation was used with rate-dependent parameters to model the failure of structural adhesive joints under mode I loading. In that study, the parameters for the cohesive law were directly determined from experiments. As reported in [19], experiments on pressure-sensitive adhesives were dominated by the rate-dependent interfacial properties, rather than the bulk viscoelasticity. Hence, the general agreement in the literature asserts the existence of rate-dependent fracture response in polymer-based interfaces. It can also be concluded that the overall rate dependence can arise as a consequence of the bulk material's behavior, of the interface response itself, or due to both.

The commonly utilized mathematical approach to study the interface fracture considers cohesive zone modeling [20]. To account for the complex microscopic processes that give rise to the new traction-free surfaces, cohesive zone models practically rely on the description of the traction-separation relationships. Such descriptions are phenomenological- but could be related to atomistic or molecular mechanisms [21, 22, 23]. Incorporating cohesive zones to model the interfaces of different materials, several research groups have demonstrated the capability of cohesive zone model (CZM) to track the complex crack propagation path [24, 25, 26, 27, 28, 29, 30, 31, 32, 33], which otherwise could only be seen via tedious experiments. In particular, as reported in [32] an elastic-plastic kinematic description was introduced to describe the irreversible separation-sliding behavior at the interface. Assum-

ing the two contacting bodies as rigid, a yield function-based approach was proposed to describe the traction-separation behavior for both normal and tangential directions. Many of the rate-dependent cohesive zone models were developed under the assumption that the rate dependence arises only due to dissipation at the interfaces [34, 5, 35]. One of the approaches focused on developing phenomenological constitutive laws that represent the cohesive strength and fracture energy as a function of opening/sliding rate at the interface [36, 37, 38]. These cohesive zone models are computationally less expensive than the models that assume a viscoelastic material ahead of the crack tip. However, most of these models were developed for a particular material system and loading conditions [39, 36, 40], limiting their applications. Another group of the study had considered viscoelastic material models to characterize the rate-dependent bond breakage at the interface [34, 41, 42, 43]. The third group adopted viscoplasticity to capture the inelastic sliding separation at the interface prior to failure [44, 35]. The present work introduces a rate-dependent cohesive zone model designed for the fracture of polymeric interfaces. The presented cohesive zone model takes into consideration both reversible elastic and irreversible rate-dependent separation sliding deformation at the interface. The viscous dissipation resulting from irreversible opening at the interface is depicted through elastic-viscoplastic kinematics, incorporating the influence of strain rate. In the present work, we focus on the uncertainty associated with the estimation of a large number of parameters of the cohesive interface model. The present viscoplastic cohesive zone model has a greater number of parameters compared to the standard linear elastic case. Further, the parameters of the present cohesive zone model cannot be obtained through macroscopic fracture experiments.

The commonly used approach of inversely identifying the cohesive zone parameters through least square fitting is often inaccurate in the case of limited experimental data due to the complexity of the model. Another common approach to identifying the parameters, especially when the number of parameters is large, is the trial and error approach. However, a trial and error approach to inversely identify a large number of parameters of a complex model is not systematic and may require a large number of evaluations of the model since the

number of all possible combinations of parameters is huge. Therefore, a systematic approach to calibrating the parameters of the cohesive zone model is necessary. A Bayesian calibration approach would alleviate the aforementioned limitations, in addition to being systematic and mathematically well-founded. Further, the existing literature is rudimentary in quantifying the uncertainty in the CZM parameter estimations and how this parameter uncertainty would propagate in the final response.

Uncertainty quantification for computational models is currently being intensely investigated since it can provide measures of confidence in the model prediction [45, 46, 47, 48, 49, 50]. Specifically, inverse calibration for parameter estimation is a key component of uncertainty quantification. Kennedy and O'Hagan have pioneered a Bayesian approach for the calibration of the unknown parameters in a computer model [51]. Their model has received significant attention as an approach for inverse calibration and is commonly referred to as the (KOH) approach. In the KOH approach, the discrepancy between the computational model and the experimental observations is modeled explicitly by a discrepancy function. The true physical process is represented as a sum of the computational model, the discrepancy function, and the observational error. The computational model and the discrepancy function are treated independently and their priors are assumed to be Gaussian processes. The observational errors are assumed to be zero mean Gaussians independent of each other. The posterior distributions of unknown model parameters and the discrepancy function parameters are estimated simultaneously using a Bayesian approach. Once these posterior distributions are estimated, the experimental observations can be predicted along with the uncertainties associated with the predictions.

The KOH approach has been extensively investigated and further extended by several studies. A statistical approach (following the KOH approach) to combine scant field observations with simulation data for calibrating the unknown parameters in the simulation model and performing uncertainty quantification was demonstrated in [52]. In another work, Higdon *et. al.* [53] extended the KOH framework for computer simulations with multidimensional output. To overcome the challenges of size and the multivariate nature of the data,

dimensionality reduction was performed using basis representations. A hierarchical Gaussian process model to combine data from multiple experiments with varying accuracies based on the KOH framework was introduced in [54]. This model made use of the more abundant but less accurate data along with the less abundant high-accuracy data to produce predictions closer to the high-accuracy experiments. Arend *et. al.* [55, 56] illustrated the problem of identifiability, *i.e.* whether the effects of calibration parameters and discrepancy function are distinguishable from one other in the model updating formulation and proposed a method to improve identifiability. An approach to calibrate the discrepancy function across different experimental settings based on the KOH framework was proposed in [57]. A decoupled approach was introduced in which the unknown parameters of the computer model are estimated independently and prior to the estimation of the discrepancy function. This modular approach was computationally more feasible and it improved identifiability. Several other noteworthy works based on the KOH framework are reported in [58, 59, 60, 61].

The aforementioned Bayesian frameworks were employed for uncertainty quantification of diverse physics-based models such as plasticity models [46, 62, 47], viscoelastic models [48], turbulence models [63], and thermal models [49, 50]. For example, Asaadi et al [62] introduced a Bayesian framework for material characterization, involving both model class selection and parameter inference, in plasticity models. The framework integrated the Bayes' rule, surrogate modeling, principal component analysis, and nested sampling techniques. These works in the literature clearly demonstrate the potential of the Bayesian approach in quantifying uncertainties and calibrating parameters to improve the physics-based computational model.

Based on the current state-of-the-art, the objective of the present work is to perform uncertainty quantification for a phenomenological rate-dependent cohesive zone model. The proposed CZM is specifically designed to model the fracture response of the polymeric interfaces, based on an elastic-viscoplastic kinematical description. To enhance the robustness and accuracy of the proposed CZM prediction, uncertainty quantification of the model is further performed. To facilitate the inverse identification of the model parameters from limited experimental data the present study considers a Bayesian calibration approach. A sensitivity

analysis is also performed to better understand the effects of inputs on the outputs of the CZM.

To summarize, calibration and uncertainty quantification of a complex model is challenging and largely unexplored for the present rate-dependent cohesive zone fracture model. The key challenges are:

1. High complexity of the model and the associated high computational cost.

2. Effects of uncertainty in the parameters and in the model are not distinguishable from one other in general.

3. Experimental data to calibrate such complex cohesive zone models is often limited or unavailable.

In this work, we tackle these challenges by the following approaches:

1. By learning surrogate/simplified models we significantly reduce the computational cost of the forward model, enabling us to perform Bayesian calibration and uncertainty quantification efficiently.

2. We adopt a modular Bayesian approach that calibrates the parameters prior to learning the discrepancy function which improves identifiability.

3. We employ a Bayesian approach to overcome the challenge of limited experimental data. By incorporating the prior knowledge about these parameters, a posterior distribution of parameters is learned through the Bayesian calibration approach that alleviates the bias due to insufficient data.

The rest of this paper is organized as follows: In Sec. 2 the rate-dependent cohesive zone model for the polymeric interfaces is described, followed by an analytical implementation of the model in Sec. 3. Bayesian calibration, Uncertainty quantification, and Sensitivity analysis of the CZM are presented in Sec. 4 and Sec. 5 followed by concluding remarks in Sec. 6

2. A Rate-dependent Phenomenological Cohesive Zone Model for Polymer Interfaces

2.1. Kinematics

In the present work, a rate-dependent traction-separation law has been proposed assuming a finite elastic-viscoplastic deformation of the polymer interfaces. In addition to that, a post-peak damage model has also been incorporated to model the degradation along the interfaces beyond post-yielding. The model has been proposed for a coupled normal and tangential (mixed mode) interfacial behavior along the interfaces. The phenomenological model stems from the work by Su et al. [32], as mentioned in the introduction. The present work extends the model to incorporate a viscoplastic component to capture the rate-dependent behavior of the interfaces. Figure 1 represents the schematic of an interface undergoing finite opening and sliding.
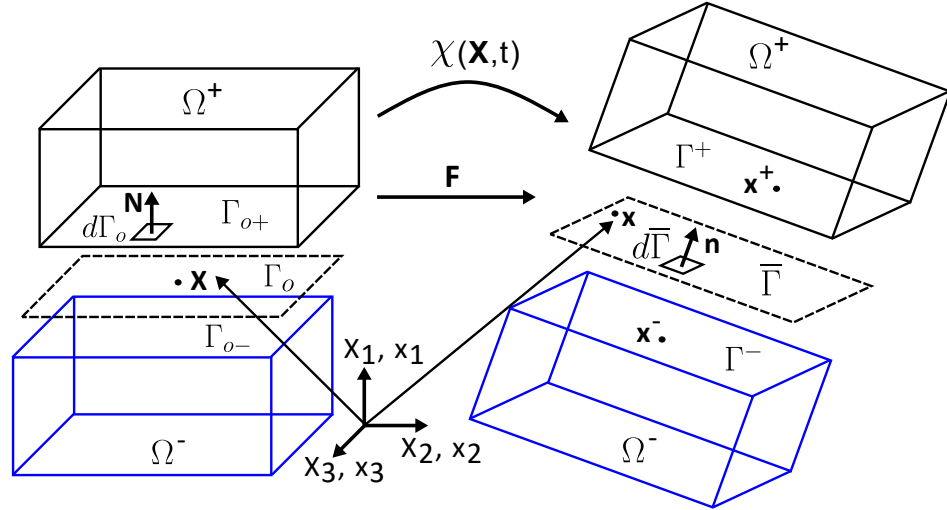
Figure 1: Schematic of an interface between two bodies Ω^+ and Ω^-.

Let us assume two bodies of polymeric materials Ω^+ and Ω^- separated by an interface Γ_o in the reference configuration as shown in Figure 1. The lower and upper surfaces are denoted as Γ_{o-} and Γ_{o+}, respectively. In the reference configuration, the surfaces Γ_{o-} and Γ_{o+} are assumed to be identical to the reference interface Γ_o where $\mathbf{X}_i$ represents the Cartesian material coordinates.

$$\Gamma_o = \Gamma_{o-} = \Gamma_{o+}, \quad \Gamma_o = \Gamma_o(\mathbf{X}_i) \tag{1}$$

In the current configuration, Γ_{o+} and Γ_{o-} become Γ^+ and Γ^-, respectively. A material point $\mathbf{X}$ initially on the interface Γ_o in the reference configuration, is located on $\Gamma^\pm$ by the motion characterized by the displacement field $\mathbf{u}$ at time $t \in T$, where T represents the time at which the deformation is applied.

$$\mathbf{x}^\pm = \mathbf{X} + \mathbf{u}^\pm, \quad \Gamma_o \to \Gamma^\pm, \quad \forall t \in T \tag{2}$$

where $\mathbf{x}^\pm$ denotes the material points on the upper and lower surfaces in the current configuration. Following the approach considered in [64] and [65], an interface Γ is introduced in the current configuration to connect the strong discontinuities across the contacting surfaces consistently. The location of a material point $\mathbf{x}$ on the interface Γ, is defined by the uniquely invertible deformation map χ, as,

$$\mathbf{x} = \chi(\mathbf{X}, t), \quad \Gamma_o \to \Gamma, \quad \forall t \in T$$
$$\mathbf{x} = \frac{1}{2}(\mathbf{x}^+ + \mathbf{x}^-), \quad \forall \mathbf{x}^\pm \in \Gamma^\pm \tag{3}$$

Following which, the deformation gradient tensor $\mathbf{F}$ is defined as:

$$\mathbf{F} = \frac{\partial \chi(\mathbf{X}, t)}{\partial \mathbf{X}}, \quad \forall \mathbf{X} \in \Gamma_o, \quad \forall t \in T \tag{4}$$

Hence, one can write that the interface Γ_o with unit normal $\mathbf{N}$ is rotated and deformed to the interface Γ having unit normal $\mathbf{n}$ in the current configuration by the following mapping:

$$\mathbf{n} = (d\Gamma_o/d\Gamma)\mathbf{F}.\mathbf{N} \tag{5}$$

In a 3D representation, the cohesive zone is assumed to be a surface where displacement discontinuities occur as displacement jumps. Let us assume, $\boldsymbol{\delta}$ as the total displacement jumps across the cohesive interface. The displacement jump vector is defined by the following expression:

11

$$\boldsymbol{\delta} = \mathbf{x}^+ - \mathbf{x}^-, \quad \forall \mathbf{x}^\pm \in \Gamma^\pm, \quad \forall t \in T \tag{6}$$

2.2. Constitutive description for the traction-separation behavior

Again, considering the framework in Su et. al [32], an additive decomposition for the displacement jump vector is introduced as,

$$\boldsymbol{\delta} = \boldsymbol{\delta}^e + \boldsymbol{\delta}^p \tag{7}$$

where, $\boldsymbol{\delta}^e$ stands for the elastic displacement jump and $\boldsymbol{\delta}^p$ is the plastic, irreversible component of the same. To account for the rate-dependent inelastic behavior of the interface, a viscoplastic constitutive framework combined with a hardening and damage behavior is considered in the present work. The hardening behavior of the cohesive surface partially accounts for the defect evolution along the interfaces. To account for the post-yield damage in the interface, a scalar damage model is also considered.

Assuming, ϕ as the free energy per unit surface area in the reference configuration, based on a purely mechanical deformation, ϕ can be expressed as:

$$\phi = \hat{\phi}(\boldsymbol{\delta}^e, \kappa, D) \tag{8}$$

where κ is a hardening variable, often expressed in terms of equivalent plastic strain/displacement. κ describes the evolution of the interface yield surface and D is the scalar damage variable. The time derivative of the free energy function is then given by,

$$\dot{\phi}(\boldsymbol{\delta}^e, \kappa, D) = \frac{\partial \phi}{\partial \boldsymbol{\delta}^e}.\dot{\boldsymbol{\delta}}^e + \frac{\partial \phi}{\partial \kappa}\dot{\kappa} + \frac{\partial \phi}{\partial D}\dot{D} \tag{9}$$

Further, following the thermodynamic consistency, the dissipation inequality can be written as,

$$\boldsymbol{t}.\dot{\boldsymbol{\delta}} - \dot{\phi} \geqslant 0 \tag{10}$$

where $\boldsymbol{t}$ is the traction vector. Using equation (7) and (9) in the dissipation inequality we get,

$$\left(\boldsymbol{t} - \frac{\partial \phi}{\partial \boldsymbol{\delta}^e}\right).\dot{\boldsymbol{\delta}} + \frac{\partial \phi}{\partial \boldsymbol{\delta}^e}\dot{\boldsymbol{\delta}}^p - \frac{\partial \phi}{\partial \kappa}\dot{\kappa} - \frac{\partial \phi}{\partial D}\dot{D} \geqslant 0 \tag{11}$$

12

In order to satisfy the inequality for any arbitrary displacement jump, we pose,

$$\left(\boldsymbol{t} - \frac{\partial \phi}{\partial \boldsymbol{\delta}^e}\right).\dot{\boldsymbol{\delta}} = 0 \tag{12}$$

Hence, the elastic traction-separation law for the cohesive interface can be obtained as,

$$\boldsymbol{t} = \frac{\partial \phi}{\partial \boldsymbol{\delta}^e} \tag{13}$$

and the dissipation becomes,

$$\frac{\partial \phi}{\partial \boldsymbol{\delta}^e}\dot{\boldsymbol{\delta}^p} - \frac{\partial \phi}{\partial \kappa}\dot{\kappa} - \frac{\partial \phi}{\partial D}\dot{D} \geqslant 0 \tag{14}$$

Following equation (14), a quadratic form of the free energy function is chosen as,

$$\phi = \frac{1}{2}(1 - D)\boldsymbol{\delta}^e.\boldsymbol{K}.\boldsymbol{\delta}^e + H\kappa^2 \tag{15}$$

where the coefficient $H > 0$ represents the hardening modulus and the matrix $\boldsymbol{K}$ denotes the interface elastic stiffness tensor as given by,

$$\boldsymbol{K} = K_N \boldsymbol{n} \otimes \boldsymbol{n} + K_T(\boldsymbol{1} - \boldsymbol{n} \otimes \boldsymbol{n}) \tag{16}$$

with $K_N > 0$ and $K_T > 0$ are the normal and tangential elastic stiffness moduli respectively. Following equation (13) the local traction vector is given by,

$$\boldsymbol{t} = (1 - D)\boldsymbol{K}\boldsymbol{\delta}^e = (1 - D)\boldsymbol{K}(\boldsymbol{\delta} - \boldsymbol{\delta}^p) \tag{17}$$

The interface traction $\boldsymbol{t}$ can be decomposed into normal component $\boldsymbol{t}_N$ and tangential component $\boldsymbol{t}_T$ as,

$$\boldsymbol{t} = \boldsymbol{t}_N + \boldsymbol{t}_T$$

$$\boldsymbol{t}_N \equiv (\boldsymbol{n} \otimes \boldsymbol{n})\boldsymbol{t} = (\boldsymbol{t}.\boldsymbol{n})\boldsymbol{n} \equiv t_N\boldsymbol{n} \tag{18}$$

$$\boldsymbol{t}_T \equiv (\boldsymbol{1} - \boldsymbol{n} \otimes \boldsymbol{n})\boldsymbol{t} = \boldsymbol{t} - t_N\boldsymbol{n}$$

where t_N stands for the magnitude of normal stress at the interface. The magnitude of the equivalent tangential stress can be further written as:

$$\tau \equiv \sqrt{\boldsymbol{t}_T.\boldsymbol{t}_T} \tag{19}$$

Here, τ is denoted as effective tangential traction. It is important to note that the displacement jump vector $\boldsymbol{\delta}$ has two components $\boldsymbol{\delta}_N$ and $\boldsymbol{\delta}_T$ corresponding to normal and tangential cohesive opening respectively.

In the 2D stress plane, the elastic domain of the cohesive constitutive law is defined as the interior of the convex yield surfaces. Once the applied interfacial displacements exceed the yield criteria, the response is governed by the choice of the yield function and the plastic flow rule. For a coupled normal and tangential cohesive behavior, the yield function is chosen as,

$$\phi_Y = \tau + \mu \langle t_N \rangle - S_{yp} \tag{20}$$

where, $\langle t_N \rangle = 0.5 * (t_N + |t_N|)$ and S_{yp} is the current yield strength, and μ is the friction coefficient. The yield strength evolution is given by the hardening law as,

$$S_{yp} = S_0 + H.\kappa \tag{21}$$

where S_0 is the initial yield stress and κ is the hardening variable.

2.3. Viscoplastic interface behavior, hardening law, and the post-yield damage

In order to define the evolution laws for the internal variables associated with the dissipative phenomena, we need to define the flow rules for the plastic displacement jump $\boldsymbol{\delta}^p$, hardening variable κ and damage variable D. As mentioned earlier, to model the rate-dependent interface behavior, a visco-plastic flow rule is adopted to describe the inelastic displacement jump as,

$$\dot{\boldsymbol{\delta}^p} = \dot{\gamma}_{vp} \boldsymbol{m}_{flow} \tag{22}$$

with the plastic flow direction given by,

$$\boldsymbol{m}_{flow} = \frac{1}{\sqrt{1 + \mu^2}} \left(\frac{\boldsymbol{t_T}}{\tau} + \mu \boldsymbol{n} \right) \tag{23}$$

For a pure mode-I case, the 1st term in the bracket is led to zero and the flow direction is governed by the normal of the deformed interface. Similarly, the second term vanishes for pure shear loading, and the plastic flow direction is governed by tangential separation.

For the viscoplastic strain rate parameter γ_{vp}, a viscoplastic flow rule is considered as,

$$\dot{\gamma}_{vp} = \gamma_o \, exp\left(-\frac{Q}{k\theta}\left[1 - \frac{\tau + \mu\langle t_N\rangle}{S_{yp}}\right]^{1/m}\right) \tag{24}$$

where γ_0 is the reference plastic strain parameter, Q is the activation energy, m is the rate sensitivity parameter, k is the Boltzmann constant and θ is the reference temperature. As explained earlier, the rate-dependent behavior of the cohesive interfaces is critical to predicting the bi-material interface failure subjected to high rate loading. In polymeric materials, inelastic deformations are governed by thermally activated motions of macromolecules. Therefore, following the approach taken by Richeton et al. [66, 67] and Ames et al. [68, 69], a thermally activated relation is chosen to calculate the inelastic deformation rate as given by equation (24). It is to note that a considerably large number of visco-plastic models are found in the literature that account for plastic flow as a thermally activated process incorporating the temperature, strain, and the strain rate effects [70, 71, 72]. Most of these models predict reasonably well the variation of the plastic strength as a function of temperature and strain rate within a limited range. However, it is seen that these models do not account for the sudden increase in yield stress at extremely high strain rates [66]. The flow rule in equation (24) is motivated by the approach taken by Richeton et al. [67, 66]. Their model is developed based on the "co-operative" model of Fotheringham and Cherry [73, 74] which assumes that the flow in the polymer is allowed when several polymer chain segments are moving in a 'co-operative' manner. A similar flow rule has also been adopted by Ames et al. [69]. They have demonstrated that such a viscoplastic model can predict the yield strength variation over a wide range of temperature and strain rates for amorphous polymers. In the present study, the assumption is that such a flow rule is adequate to predict the rate-dependent yield behavior of a thin layer of polymer adhesives as well.

An evolution equation is further defined to describe the hardening variable κ, as

$$\dot{\kappa} = \dot{\gamma}_{vp}\frac{\partial\phi_Y}{\partial S_{yp}} \tag{25}$$

In order to model the damage initiation and progression along the interface in the post-yield regime, the damage is assumed to be uncoupled from the plastic deformation. A simple
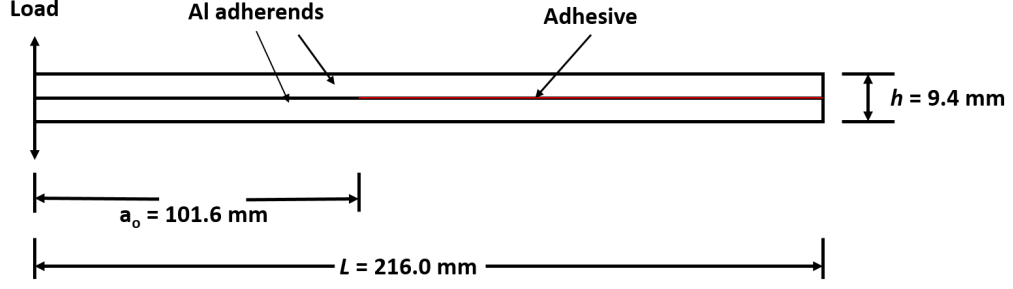
Figure 2: Geometry of the experimental DCB specimen as per [5];

damage rule, based on the total effective displacement is used as,

$$D = \frac{\delta^f(|\delta| - \delta^0)}{|\delta|(\delta^f - \delta^0)} \text{ for } \delta^0 < |\delta| \leqslant \delta^f \tag{26}$$

where δ^0 and δ^f are the effective displacement jump at the onset of damage and at the final failure of the interface, respectively; $|\delta|$ represents the effective displacement jump defined as $|\delta| = \sqrt{\delta_N^2 + \delta_T^2}$.

3. Numerical implementation of the CZM

To predict the interfacial failure of structural components, the proposed CZM is evaluated analytically to predict the mode-I interface failure. This analytical implementation considers a mode-I fracture geometry consisting of a 2-D double cantilever beam (DCB) specimen with an initial notch as shown in Figure 2. We assume that the beams in the DCB geometry are almost rigid (≈ 1000 times stiffer) compared to the interface and the entire deformation only happens across the interface. This assumption helps to implement the CZM analytically. However, it is to be noted that the response of the beams may play a role and must be considered for practical purposes. Nevertheless, the results of the present method will remain unchanged as long as the interface is much weaker than the bulk and failure happens at the cohesive interfaces. Model predictions are performed for three different displacement rates 5.08, 50.8, and 508.0 mm/min, respectively.

For the analytical implementation, the tangential sliding of the interface is ignored and the friction coefficient is assumed as ($\mu = 1$) to ensure the no-slip condition. Assuming the

16

cantilevers as perfectly rigid, the (normal) opening along the interface line at any point x from the pivot point can be estimated as, $\delta_N(x) = \frac{x}{L}\Delta$, where L is the interface length, and Δ is the crack opening displacement along the applied load line as shown in Figure 3. Balancing the moment exerted by the cohesive force generated due to the interface traction
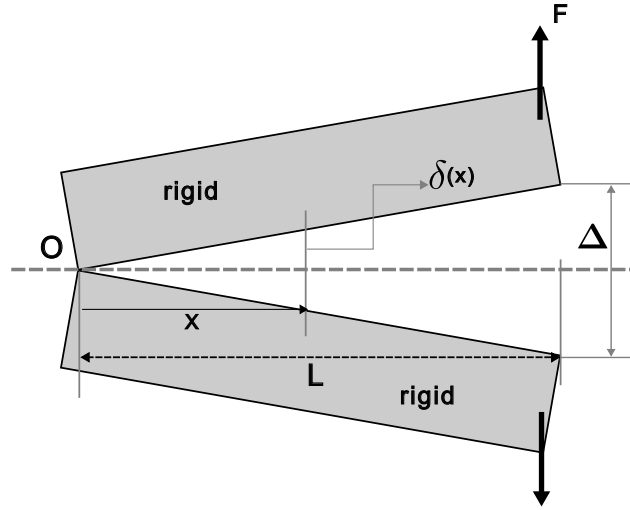
Figure 3: Schematic of the rigid double cantilever beam under mode-I opening;

with the external moment due to the applied force F about the pivot point "O" we get,

$$B \int_0^L x t_N(x) dx = LF \qquad (27)$$

where B is the specimen width and $t_N(x)$ denotes the (normal) traction at point "x". The traction $t_N(x)$ is also a function of the interface opening at a distance x, as $t_N(\delta_N(x))$. It is also to be noted that the traction-separation law as described earlier is nonlinear in nature. Hence the closed-form integration for the moment balance equation is not trivial. Therefore, we numerically discretize the interface into a finite number of surface elements (in this case 1000) and calculate the traction distribution $(t_{N1}, t_{N2} \ldots t_{N1000})$ for those elements in a discrete manner for a given displacement Δ. These values are then used in the moment balance equation to calculate the applied external force F.

The assumption of the "rigid"ness of the bulk material in our analytical calculation considers the deformation only to happen across the interface. To incorporate the bulk deformation

of the cantilever beams in the experiments, one needs to implement the CZM in a finite element framework which has not been considered in the present work. The focus of the present work is to consider the uncertainty associated with the model calibration in a rate-dependent phenomenological cohesive interface model in order to improve the accuracy and robustness of the model. Hence, we have only considered an analytical implementation of the proposed traction-separation law in a pure mode I condition and ignored the bulk material deformation. In our analytical calculation, the thickness of the adhesive layer is considered zero. In principle, it is possible to extend the present model by considering a finite-thickness cohesive layer and use finite element analysis to solve for the failure behavior.

To inversely determine the cohesive interface parameters a Bayesian calibration is performed. The inverse calibration of parameters, from limited experiments always poses a non-uniqueness in the parameter estimation. The uncertainty associated with the model parameter estimation affects the accuracy of the model predictions for which experimental data is not available to verify. In addition, determining the model parameters through the inverse trial-error process is computationally tedious, even for simple mode-I analytical calculation and the simulation time is a major bottleneck in the implementation of the model. Hence, a Bayesian estimation approach is proposed to calibrate the CZM parameters using limited experimental data.

4. Bayesian calibration and uncertainty quantification

4.1. Details of the experiment

In the original experiments [5], rate-dependent debonding of a polyethylene-based adhesive was studied using a double cantilever beam (DCB) set-up, similar to the geometry as shown in Figure 2. The test specimen consists of Al601-T6 adherends bonded with a thermoplastic high-density polyethylene-based adhesive. Each adherend was 216 mm long, 4.70 mm thick, and 25 mm wide. The specimen contains an initial crack length of 101.6 mm, as shown in Figure 2. During the experiments, displacement had been applied at the loading points along the direction indicated by arrows. The fracture behavior of the specimens

was investigated and load-crack opening displacements were recorded at different cross-head displacement rates as 5.08, 50.8, and 508.0 mm/min, respectively. Further details on the experiments can be found in [5].

4.2. Calibration of model parameters using a Bayesian approach

In general, computational models like the CZM take inputs $\mathbb{X}$ (strain rate and displacement in the CZM) to predict the quantities of interest $\boldsymbol{Y}$ (load at the specified displacement in the CZM). Where the inputs $\mathbb{X}$ to the model can be random or deterministic. Most computational models have unknown parameters $\boldsymbol{\Theta}$ (parameters provided in Table. 2 for the CZM) that need to be calibrated. Bayesian calibration is a powerful, mathematically well-founded, and widely used method for identifying these unknown parameters of the computational model. Bayesian calibration systematically incorporates the prior knowledge about the parameters and it overcomes the ad-hoc nature of the trial-and-error approach. In this work, the unknown parameters of the cohesive zone model are obtained through Bayesian calibration as explained in the following section.

4.2.1. The Bayesian Calibration method

For the purpose of Bayesian calibration and uncertainty quantification, the experimental response ($\boldsymbol{Y}^{(e)}$) can be modeled following the Kennedy and O'Hagan approach [51] as:

$$\boldsymbol{Y}^{(e)} = \boldsymbol{Y}^{(c)}(\mathbb{X}, \boldsymbol{\Theta}) + \boldsymbol{\delta}_{disc}(\mathbb{X}) + \boldsymbol{\epsilon} \tag{28}$$

where,

$\boldsymbol{Y}^{(c)}(\mathbb{X}, \boldsymbol{\Theta})$ is the response from the computational model,

$\boldsymbol{\delta}_{disc}(\mathbb{X})$ is the discrepancy between the model and the experimental response,

$\boldsymbol{\epsilon}$ is the uncertainty in the measurements of experimental response.

Owing to their computational efficiency, we use a modular approach [57] to calibrate the unknown parameters, $\boldsymbol{\Theta}$, of the CZM in this work. In this approach, the Bayesian calibration is performed separately and prior to the estimation of the discrepancy function. Thus, parameter uncertainty and measurement errors are quantified during calibration, while uncertainty

due to modeling error is incorporated through the discrepancy function after the calibration. Thus, the experimental response is written as,

$$Y^{(e)} = Y^{(c)}(\mathbb{X}, \Theta) + \epsilon \tag{29}$$

Where, the measurement error (ϵ) is modeled as a zero mean Gaussian, $\epsilon \sim N(0, \Sigma)$, with covariance Σ.

Therefore, the experimental response $Y^{(e)}$ is Gaussian with mean $Y^{(c)}(\mathbb{X}, \Theta)$ and covariance Σ.

$$Y^{(e)} \sim N(Y^{(c)}(\mathbb{X}, \Theta), \Sigma) \tag{30}$$

The unknown parameters Θ in equation (30) can be estimated using a Bayesian approach. Given a prior distribution of the unknown model parameters $p(\Theta)$ and a set of experimental observations d, the posterior distribution of Θ can be estimated from Bayes theorem as follows:

$$p(\Theta|d) = \frac{p(d|\Theta)p(\Theta)}{p(d)} \tag{31}$$

The posterior distribution of the parameters provides the uncertainty due to the model's parameter. Here, $p(d|\Theta)$ is the likelihood of observing the data d given the parameters Θ. Given a set of n independent experimental observations $d = \{(x_1, y_1^{(e)}), (x_2, y_2^{(e)}), ...(x_n, y_n^{(e)})\}$, the likelihood function $p(d|\Theta)$ considering equation (30) can be written as,

$$p(d|\Theta) = \prod_{i=1}^{n} N(Y^{(c)}(x_i, \Theta), \Sigma) \tag{32}$$

$$= \prod_{i=1}^{n} \frac{1}{\sqrt{(2\pi)^{N_{out}} det(\Sigma)}} \exp\left(-\frac{1}{2}(y_i^{(e)} - y_i^{(c)})^T \Sigma^{-1}(y_i^{(e)} - y_i^{(c)})\right) \tag{33}$$

With this likelihood function and a prior distribution of calibration parameters, Θ, the posterior distributions can be estimated from equation (31). In cases where the measurement error (ϵ) is unknown apriori, as in this work, the covariance matrix Σ can be jointly estimated along with the unknown parameters θ. In this work, a diagonal covariance is assumed $\Sigma = \sigma^2 I_{N_{out}}$. Thus, the likelihood function can be written as,

$$p(d|\Theta, \sigma^2) = \prod_{i=1}^{n} \frac{1}{\sqrt{(2\pi\sigma^2)^{N_{out}}}} \exp\left(-\frac{1}{2\sigma^2}(y_i^{(e)} - y_i^{(c)})^T(y_i^{(e)} - y_i^{(c)})\right) \tag{34}$$

and the joint posterior distribution is

$$p(\mathbf{\Theta}, \sigma^2 | \boldsymbol{d}) = \frac{p(\boldsymbol{d}|\mathbf{\Theta}, \sigma^2)p(\mathbf{\Theta})p(\sigma^2)}{p(\boldsymbol{d})} \qquad (35)$$

This joint distribution can be marginalized to obtain the posterior distribution of unknown parameters and the measurement error. However, the term $p(\boldsymbol{d})$ is a normalizing constant that involves a high dimensional integral and thus is intractable which in turn makes the posterior distribution in equation (31) and (35) intractable. Therefore, the posterior distribution is approximated via a Markov Chain Monte Carlo (MCMC) method as described in Sec. 4.2.3. In the following, we describe at first the prior distributions of the parameters considered here.

Parameter	Prior	
	Distribution	Parameters
Normal stiffness, K_N (MPa/mm)	Gaussian	$[240, 40]$
Displacement at the onset of damage, δ^0 (mm)	Uniform	$[0, 10]$
Displacement at final failure, δ^f (mm)	Uniform	$[10, 20]$
Hardening modulus, H (MPa/mm)	Gaussian	$[58, 9.67]$
Normal yield strength, S_o (MPa)	Gaussian	$[60.7, 10.12]$
Reference plastic strain, γ_o (mm/s)	Gaussian	[1e-6,0.33e-6]
Activation energy, Q (N-mm)	Gaussian	[1.5e-19,0.5e-19]
Rate sensitivity parameter, m	Gaussian	$[25, 4.17]$

Table 2: Prior distribution of parameters used for Bayesian calibration

4.2.2. Prior distribution of parameters

The prior distribution of parameters represents our prior knowledge or assumptions about the parameter and they play a key role in Bayesian inference problems. The prior distribution has minor effects on the posterior when the experimental data is sufficiently large in number. Whereas, when the data is limited, as in the case of this work, the prior distribution of

parameters plays a significant role in determining the posterior of parameters. Therefore it becomes crucial to make reasonable choices for the prior distribution.

The most common choices for the prior distribution are the non-informative uniform distribution and the informative Gaussian distribution. Uniform distribution for the parameters is assumed when no information about the parameter is available. Since the support of the uniform distribution is bounded, one has to be careful in choosing the bounds of the uniform distribution. On the other hand, if a value of the parameter is approximately known a Gaussian distribution can be assumed with the mean at that value. In this work, when the bounds of the parameters are known a priori and when no information about these parameters is available in the literature we use a uniform prior. For all other parameters, a Gaussian prior is chosen. For example, in case of displacement at damage onset and final failure, we know a priori that the value of this parameter cannot be lower than zero and it cannot exceed the maximum strain applied in the experiments. Therefore, a uniform prior is chosen for these parameters. Detailed information on the selection of priors is as follows:

Normal stiffness, K_N: A Gaussian distribution is assumed for the parameter K_N. The parameters of the Gaussian distribution are evaluated from the experimental response of tough polyethylene in [75]. The slope of the traction separation curves for the polyethylene (PE2) is taken as the mean of the Gaussian and the standard deviation is assumed one-sixth of the mean [1].

Displacement at the onset of damage and final failure, δ_o, δ_f: From the experimental response of the DCB experiments, the peak load occurs at 10 mm COD. Therefore, the onset of damage is assumed to occur anywhere from 0 to 10 mm and the final failure is assumed to occur anywhere from 10 to 20 mm. Due to these assumptions, uniform prior distributions are assumed for these parameters with the corresponding range of values.

Hardening modulus, H and Activation energy, Q: A Gaussian distribution is assumed for the hardening modulus and the activation energy. The parameters of the Gaussian distri-

---

[1] $\sigma = \mu/6$ is assumed so that 99.7% (or 3σ) of the samples are within $[0.5\mu \quad 1.5\mu]$.

butions are taken from a similar constitutive model used for the polycarbonate materials in [76]. The value of the hardening modulus and activation energy in [76] is used as the mean of the Gaussian with a standard deviation of one-sixth and one-third of the mean respectively.

Normal yield strength, S_o: The normal yield strength of polyethylene is taken from an online materials database for high-density polyethylene [77]. The prior distribution is assumed Gaussian with value from the database as the mean and one-sixth of this value as the standard deviation.

Reference plastic strain γ_o and Rate sensitivity parameter m: Since γ_o and m are parameters of the phenomenological model introduced in this work for characterizing the viscoplastic interface behavior, no knowledge about these parameters exists. Therefore, a minimum number of trial and error is performed to get an approximate value (or order of magnitude) for these parameters. Using these values as the mean a Gaussian distribution is assumed for these parameters and a standard deviation of one-third and one-sixth of the mean is assumed for γ_o and m respectively.

Measurement errors: Since the measurement errors are parametrized by the variance σ^2, a uniform prior for the parameter σ^2 is assumed with the range [0,1].

With these assumptions and prior knowledge, the prior distribution of the eight unknown parameters of the cohesive zone model can be summarised as given in Table. 2. It is to be noted that the support of all the parameters is constrained to be non-negative.

4.2.3. Markov Chain Monte Carlo method

We resort to an extensive and robust framework known as the Markov chain Monte Carlo (MCMC) method to evaluate the posterior distribution given in equation (35). This framework enables sampling from a broad range of distributions and demonstrates excellent scalability with the dimensionality of the sample space. A Markov chain is a random process that transitions from one state to the other such that the probability of a future state depends only on the current state [78]. In MCMC methods a Markov Chain is constructed over the support of the prior distribution such that the equilibrium distribution of the Markov Chain is equal to the posterior distribution [78, 79, 80]. In doing so, we obtain samples from the

posterior distribution by recording the states of the Markov chain. The Markov Chains can be constructed even when the normalizing constant $p(\boldsymbol{d})$ is unknown thereby making the MCMC methods suitable to approximate equation (35).

The UQLab [81] framework is used to perform the Bayesian Calibration. The CZM is integrated with the Bayesian inference module of UQLab in MATLAB for this purpose. The CZM is evaluated analytically as described in Sec. 3. The CZM acts as the forward computational model, $\boldsymbol{Y}^{(c)}(\mathbb{X}, \boldsymbol{\Theta})$, in equation (29), whose input, $\mathbb{X} \in \mathbb{R}^n$, is the displacement and the output, $\boldsymbol{Y}^{(c)} \in \mathbb{R}^n$, is the load. Here, n denotes the number of discretization points of the load-displacement curve. The value of n is chosen such that the load-displacement curve is refined enough [2]. There are eight unknown model parameters, $\boldsymbol{\Theta} \in \mathbb{R}^8$, that are calibrated.

In order to calibrate the unknown parameters, the results of the DCB experiments are used for three different strain rates, and their corresponding CZM predictions are calculated. The posterior distributions of the model parameters are computed from equation (35) by using the experimental data, the model prediction, and the prior distributions of parameters. The posterior distribution in equation (35) is intractable and thus it is approximated via an MCMC sampling method. An Affine Invariant Ensemble Algorithm (AIES) is used to obtain the posterior distribution of the unknown parameters. The posterior distribution is obtained after burning out 50% of the initial samples. Further details on the AIES algorithm are given in Appendix A.

4.2.4. Results of the Bayesian calibration

The estimates for the posterior distribution of parameters obtained through Bayesian calibration are presented in Table 3. In addition to these parameters the posterior distribution of variance in the measurement errors (σ^2) have mean $= 1$ and standard deviation $= 17e - 4, 5e - 4$ and $2.6e - 4$ for the 5, 50 and 500 mm/min strain rates respectively. It is to be noted that, there is a significant difference between the prior and posterior means of the hardening

---

[2]In this work $n = 20$ is chosen, which we found to provide sufficient refinement.

modulus (H) learned through the Bayesian calibration approach. The observed difference stems from the fact that the prior distributions are derived from existing literature, which pertains to the original hardening law. In contrast, our work introduces modifications to the hardening law. Consequently, it is expected that the corresponding parameters will undergo changes. Further, the large difference between the prior and the posterior demonstrates that the parameters obtained through the Bayesian calibration are not biased towards the prior. We utilize the mean of the posterior distributions of the parameters to perform the

Parameter	Posterior	
	Mean	Std
Normal stiffness, K_N (MPa/mm)	326.81	0.1815
Displacement at the onset of damage, δ^0 (mm)	5.83	1.72e-3
Displacement at final failure, δ^f (mm)	17.91	0.0594
Hardening modulus, H (MPa/mm)	0.3376	0.0805
Normal yield strength, S_o (MPa)	78.87	11.87
Reference plastic strain, γ_o (mm/s)	3.7e-7	5.75e-8
Activation energy, Q (N-mm)	1.58e-19	3.02e-20
Rate sensitivity parameter, m	47.06	6.01

Table 3: Mean and standard deviations of the Gaussian posteriors of Bayesian calibration

forward evaluation of the CZM. The load-displacement curves obtained through the CZM for the calibrated parameters are compared against the experiments in Figure 4, which shows a good match. Note that the load-displacement curves are truncated at 20mm COD since the experimental data showed unstable crack propagation beyond that point. The CZM could capture the linear part, the onset of failure, the peak, and the post-peak response for all the strain rates. The parameters obtained from Bayesian calibration predict the experimental response with an average error of 3.76% between the model evaluation and the experimental response. The percentage error is evaluated as $err = \frac{\sqrt{\int (y^e - y^p)^2 dx}}{\sqrt{\int (y^e)^2 dx}} \times 100$.
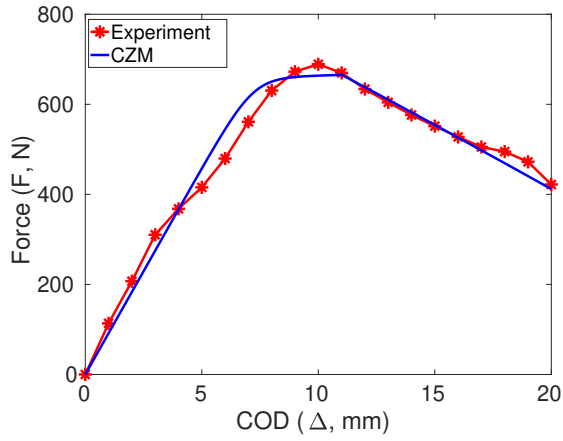
(a) 5 mm/min strain rate
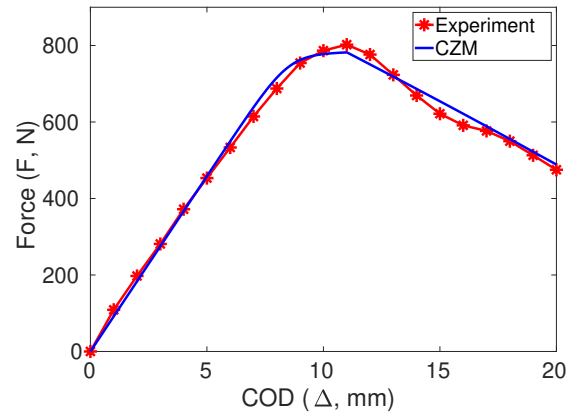
(b) 50 mm/min strain rate
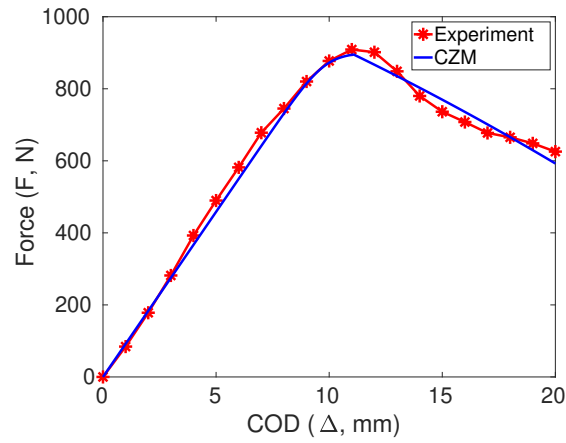
(c) 500 mm/min strain rate

Figure 4: Comparison of the load-displacement curves predicted by the CZM with the mean of the posterior distribution of parameters against experiments. Markers (*) indicate the experimental data points used for calibration.
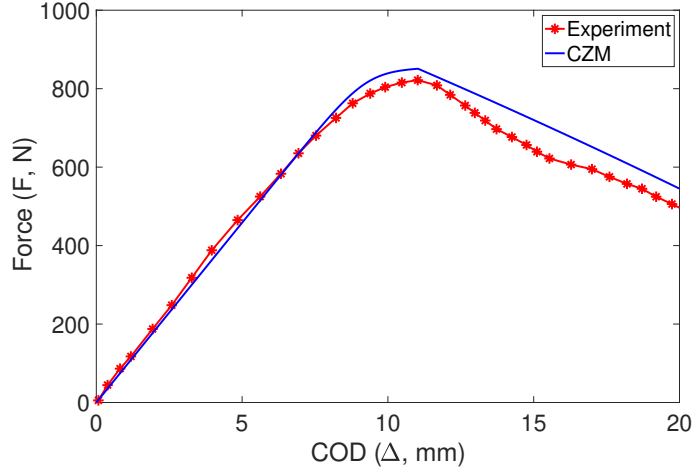
Figure 5: Validation of the parameters obtained from Bayesian calibration. Load displacement predictions for 203 mm/min strain rate. The data for this strain rate is not used during calibration.

Validation of the calibrated parameters for a test data: In order to validate the results of the Bayesian calibration approach, we have used the calibrated parameters to predict the response of an experiment performed at 203 mm/min strain rate. The experimental response at this strain rate is not used during calibration. The results of the calibration are presented in Figure. 5. There is an excellent qualitative match between the experiment and the prediction. The error in the prediction is 10.3%, which is quite good considering that the strain rates used in the calibration are far from this test data. Most of the errors are in the post-peak response prediction. It is to be noted that, although the presented approach should work in principle for any strain rate, one should use caution while extrapolating to strain rates far away from the ones present in the experiments and used in validation since the results might be erroneous.

Trace and density plots for the 100 randomly initialized MCMC chains for the normal stiffness parameter, K_N, are shown in Figure 6. These plots are necessary tools to assess the convergence of the MCMC chains. Trace plots depict the evolution of the MCMC chains over the steps and the density plot shows the probability densities of the MCMC chains. The trace plot shows that the randomly initialized chains have all converged to the same distribution after 5000 steps. The small standard deviation of the density plot depicts a low

27

level of uncertainty in the parameter K_N after the calibration. The details for the rest of the parameters and further analysis on the posterior distributions of the parameters are given in Appendix B.
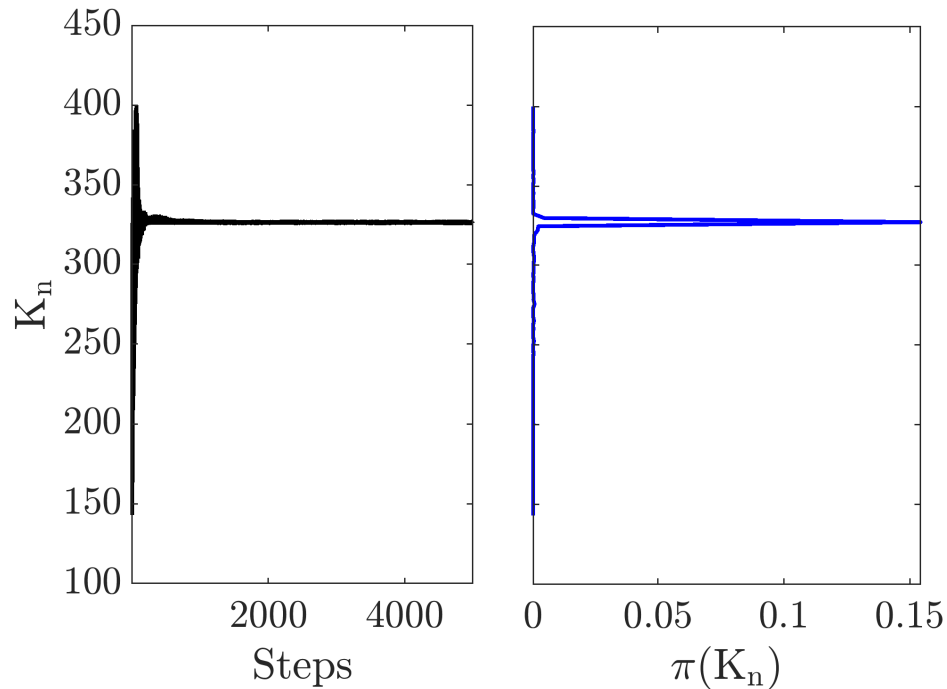
Figure 6: Trace and density plots for the K_N parameter at 5 mm/min strain rate.

Although the Bayesian calibration improves the CZM predictions, discrepancies between the experimental responses and the predictions still exist as seen in Figure 4. To further improve the model's prediction we learn a discrepancy function of equation (28), in the following section.

4.2.5. Comparison with deterministic calibration approaches

In this section, we compare the results of the Bayesian calibration approach with two deterministic calibration approaches.

In the first approach, we predict the output of the CZM with the parameters obtained from the literature (mean of the prior parameters in Table 2) as shown in Figure 7. Since the contribution of the experimental data shown in the figure is not considered to this approach, the predictions of the CZM are highly erroneous as expected. This shows the chosen prior

| (a) 5 mm/min strain rate | (b) 50 mm/min strain rate | (c) 500 mm/min strain rate |
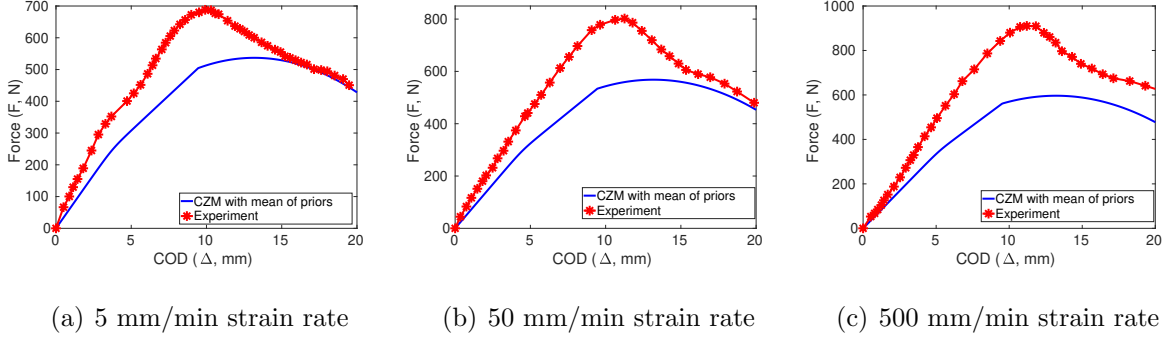
Figure 7: Evaluation of CZM for parameter values are chosen as the mean of their prior distribution.

distributions are not informed by the experiments at hand. It also demonstrates the need for Bayesian calibration.

In the second approach, we perform a non-linear minimization of the error between the CZM predictions and the experimental data to find the best set of parameters. The simplex search method [82] is used to minimize the following error function:

$$f = \sum_{r=1}^{3} \sqrt{\int (y_r^e - y_r^p)^2 dx} \tag{36}$$

where $r = 1, 2, 3$ denotes the three strain rates. The results of the CZM with the parameters obtained using the optimization method are shown in Figure 8. The nonlinear optimization approach yields better parameters than the mean of their priors. It can capture the experiments for 500 mm/min strain rate quite well. However, the error is still significantly higher for the nonlinear optimization approach as compared to the Bayesian calibration approach considering all strain rates. Further, the Bayesian calibration approach provides the uncertainty estimates naturally through the stochastic parameters which cannot be obtained by a deterministic calibration procedure such as the nonlinear optimization. This underscores the necessity for Bayesian calibration.

4.3. Discrepancy between the calibrated model and the experiment

The difference between the prediction of the computational model with the calibrated parameter and the experimental response is an important source of uncertainty. This difference

(a) 5 mm/min strain rate   (b) 50 mm/min strain rate   (c) 500 mm/min strain rate
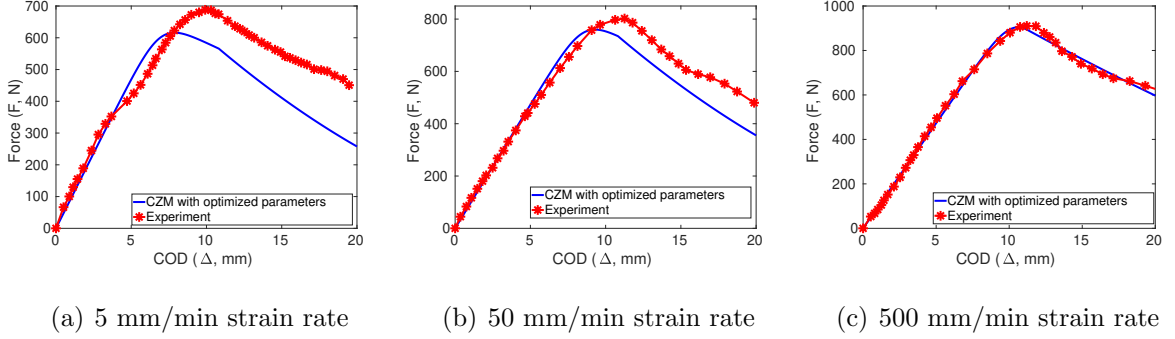
Figure 8: Evaluation of CZM for parameter values obtained through a simplex search-based optimization.

can arise due to missing physics, incorrect assumptions, numerical approximations, and/or other inaccuracies of the computational model or due to experimental variations. For example, the rate-dependent response of the interface may be coupled with the response of the bulk, which is not taken into account in this work. To account for these differences, which are a source of uncertainty, a discrepancy function is introduced. The discrepancy function together with the computational model provides better predictions of the experimental response. The functional form of the discrepancy function varies with varying applications. In this work, we learn the discrepancy function using a Gaussian process model $\mathbf{Y}_\delta(\mathbf{x}) \sim GP(\boldsymbol{\mu}_\delta, \boldsymbol{\Sigma}_\delta)$. A brief overview of Gaussian process models is presented in the following.

4.3.1. Gaussian Process models

A Gaussian Process (GP) is a collection of random variables where each random variable and any finite linear combination of these random variables follow normal distribution. A GP model is a stochastic model for the prediction of the distribution of the output variables. It assumes that the output of the model $\mathbf{Y}(\mathbf{x})$ is a realization of a GP

$$\mathbf{Y}(\mathbf{x}) \sim GP(\boldsymbol{\beta}^T \boldsymbol{f}(\boldsymbol{x}), \sigma^2 \boldsymbol{R}(\boldsymbol{x}, \boldsymbol{x}'; \hat{\boldsymbol{\theta}})) \tag{37}$$

where, $\boldsymbol{\beta}^T \boldsymbol{f}(\boldsymbol{x})$ is the mean of the GP, $\boldsymbol{f}(\boldsymbol{x}) = \{f_i; i = 1, ..., P\}$ is a array of P arbitrary functions and $\boldsymbol{\beta}$ is the array of their coefficients. $\boldsymbol{R}(\boldsymbol{x}, \boldsymbol{x}'; \hat{\boldsymbol{\theta}})$ is the correlation function with hyperparameters $\hat{\boldsymbol{\theta}}$ and σ^2 is a constant representing the variance. With this assumption,

30

the prediction $\hat{\boldsymbol{Y}}(\boldsymbol{x})$ at a new input point $\boldsymbol{x}$, given a set of known model responses $\overline{\boldsymbol{Y}} = \{\boldsymbol{y}^{(1)}, ..., \boldsymbol{y}^{(N)}\}$ at input points $\overline{\boldsymbol{X}} = \{\boldsymbol{x}^{(1)}, ..., \boldsymbol{x}^{(N)}\}$, has a joint Gaussian distribution defined by [83, 84]

$$\left\{ \begin{matrix} \hat{\boldsymbol{Y}}(\boldsymbol{x}) \\ \overline{\boldsymbol{Y}} \end{matrix} \right\} \sim N_{N+1} \left(\left\{ \begin{matrix} \boldsymbol{f}^T(\boldsymbol{x})\boldsymbol{\beta} \\ \boldsymbol{F}\boldsymbol{\beta} \end{matrix} \right\} + \sigma^2 \left\{ \begin{matrix} 1 & \boldsymbol{r}^T(\boldsymbol{x}) \\ \boldsymbol{r}(\boldsymbol{x}) & \boldsymbol{R} \end{matrix} \right\} \right) \tag{38}$$

where

$\boldsymbol{F} = F_{ij} = f_j(\boldsymbol{x}^{(i)}); \quad i = 1, ..., N; j = 1, ..., P$

$\boldsymbol{r} = r_i = R(\boldsymbol{x}, \boldsymbol{x}^{(i)}, \hat{\theta}); \quad i = 1, ..., N$

$\boldsymbol{R} = R_{ij} = R(\boldsymbol{x}^{(i)}, \boldsymbol{x}^{(j)}; \hat{\theta}); \quad i, j = 1, ..., N$

The mean and the variance of the prediction $\hat{\boldsymbol{Y}}(\boldsymbol{x})$ can be estimated as,

$$\mu_{\hat{\boldsymbol{Y}}}(\boldsymbol{x}) = \boldsymbol{f}^T(\boldsymbol{x})\hat{\boldsymbol{\beta}} + \boldsymbol{r}^T(\boldsymbol{x})\boldsymbol{R}^{-1}\left(\overline{\boldsymbol{Y}} - \boldsymbol{F}\hat{\boldsymbol{\beta}}\right) \tag{39}$$

$$\sigma^2_{\hat{\boldsymbol{Y}}}(\boldsymbol{x}) = \sigma^2 \left(1 - \boldsymbol{r}^T(\boldsymbol{x})\boldsymbol{R}^{-1}\boldsymbol{r}(\boldsymbol{x}) + \boldsymbol{u}^T(\boldsymbol{x})(\boldsymbol{F}^T\boldsymbol{R}^{-1}\boldsymbol{F})^{-1}\boldsymbol{u}(\boldsymbol{x})\right) \tag{40}$$

where,

$$\hat{\boldsymbol{\beta}} = (\boldsymbol{F}^T\boldsymbol{R}^{-1}\boldsymbol{F})^{-1}\boldsymbol{F}^T\boldsymbol{R}^{-1}\overline{\boldsymbol{Y}}; \qquad \boldsymbol{u}(\boldsymbol{x}) = \boldsymbol{F}^T\boldsymbol{R}^{-1}\boldsymbol{r}(\boldsymbol{x}) - \boldsymbol{f}(\boldsymbol{x})$$

In this work, we use this Gaussian process regression model to learn the discrepancy function.

4.3.2. Results of the discrepancy function

The mean of the posterior distributions is used to evaluate the computational model for the three strain rates. The discrepancy (δ) is calculated as the difference between the experimental response and the output of the computational model at a given input ($\boldsymbol{X}$). Three Gaussian processes, one for each strain rate, are learned for the input and the discrepancy. A zeroth-order polynomial is taken as the mean of the Gaussian process and an ellipsoidal correlation function is used. The hyperparameters of the Gaussian process are obtained by minimizing the cross-validation error. A hybrid Genetic algorithm method is used as the optimization method to obtain the hyperparameters. In making any new predictions, the output of the computational model is corrected using this discrepancy function. The number

of points on the load-displacement curve used to learn the discrepancy function is selected based on the analysis of error convergence as given in Appendix C.

The Gaussian process learned for the discrepancy between the experimental response and the model prediction is shown in Figure 9. The GP captures the discrepancy quite accurately and with minimum uncertainty at the training data points.
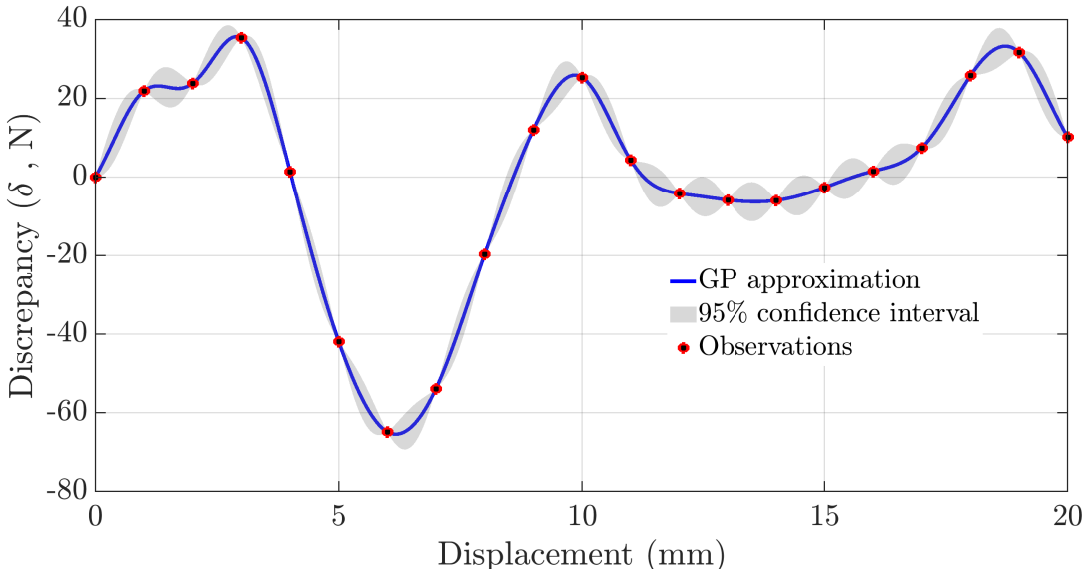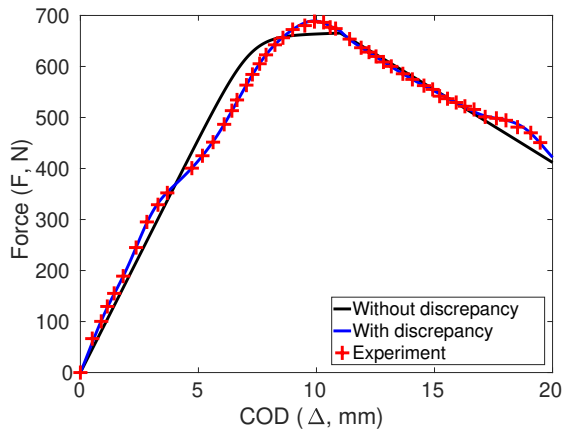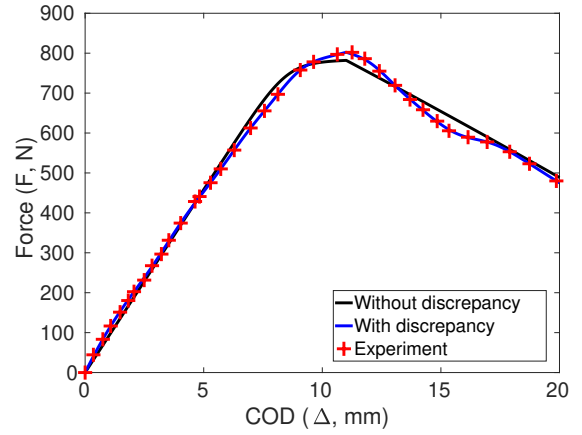

Figure 9: The discrepancy function modeled as a Gaussian process for the 5 mm/min strain rate case.

The results of the computational model augmented with the discrepancy function are presented in Figure 10. The results show that after the introduction of a discrepancy function, the model's prediction of the experimental response has improved significantly for all three strain rates. In cases where multiple experimental results are available for a given input setting, the significance of the discrepancy function is further enhanced as it captures the systematic errors in the predictions due to the assumptions in the model. To quantify the improvement in the CZM's predictions with the addition of the discrepancy function, the percentage error is evaluated and provided in table 4 below [3].

---

[3] y^p is the predictions of the CZM with or without the discrepancy function. These errors are calculated for data points that are not used to train the GP for discrepancy function.

(a) 5 mm/min strain rate

(b) 50 mm/min strain rate
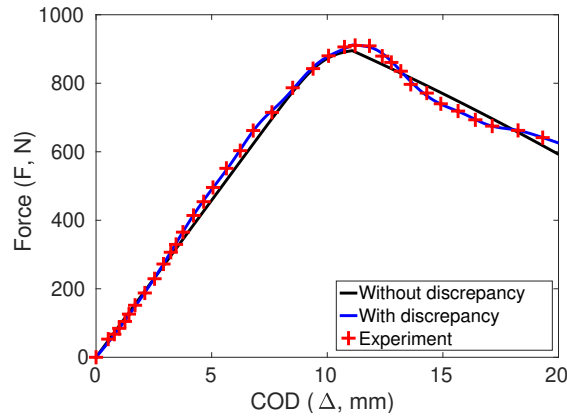
(c) 500 mm/min strain rate

Figure 10: Load-displacement curves obtained by the model with and without the discrepancy function. The experimental data used here are test points that were not used in training the GP for the discrepancy.

Strain rate	% Error CZM	% Error CZM with $\boldsymbol{\delta}$
5 mm/min	5.10	0.38
50 mm/min	2.98	0.25
500 mm/min	3.20	0.45

Table 4: Percentage error in the CZM predictions with and without the discrepancy function
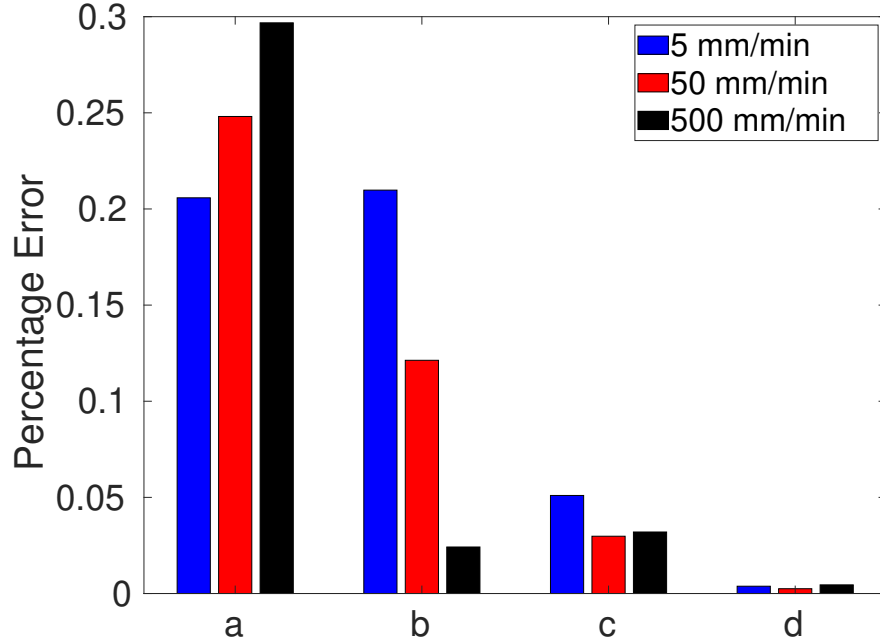
Figure 11: Comparison of errors between the experiment and the CZM model evaluated with (a) mean of the priors (b) parameters obtained by nonlinear optimization (c) mean of the posterior parameters (d) mean of the posterior with discrepancy

Comparison of the error between the CZM predictions and the experiments with parameters obtained from various calibration approaches used in this work are shown in Figure 11. This demonstrates that the calibration using standard nonlinear optimization techniques may not provide the necessary accuracy while dealing with a large number of parameters. The CZM evaluated with the mean of prior parameters performs the worst and the Bayesian calibration with the discrepancy function performs the best amongst all the compared approaches. In addition to these results, we have computed the energy release rates for the predicted load-displacement curves and presented them in Appendix E.

4.4. Uncertainty Quantification

A computational model is a mathematical representation of a physical phenomenon. Physical phenomenons have natural variability associated with them such as inherent variability in the material properties, which are referred to as aleatoric uncertainties. Further, model-

ing of these physical phenomena introduces additional uncertainties, which may be a result of limited measurement data, imprecise measurement, solution approximations, unknown model parameters, and model assumptions. These uncertainties are referred to as epistemic uncertainties. The aleatoric and epistemic uncertainties need to be modeled and quantified to better understand the reliability of the predictions of the computational models. The steps involved in quantifying uncertainties in the predictions of the CZM are summarised as a flow chart in Figure. 12.
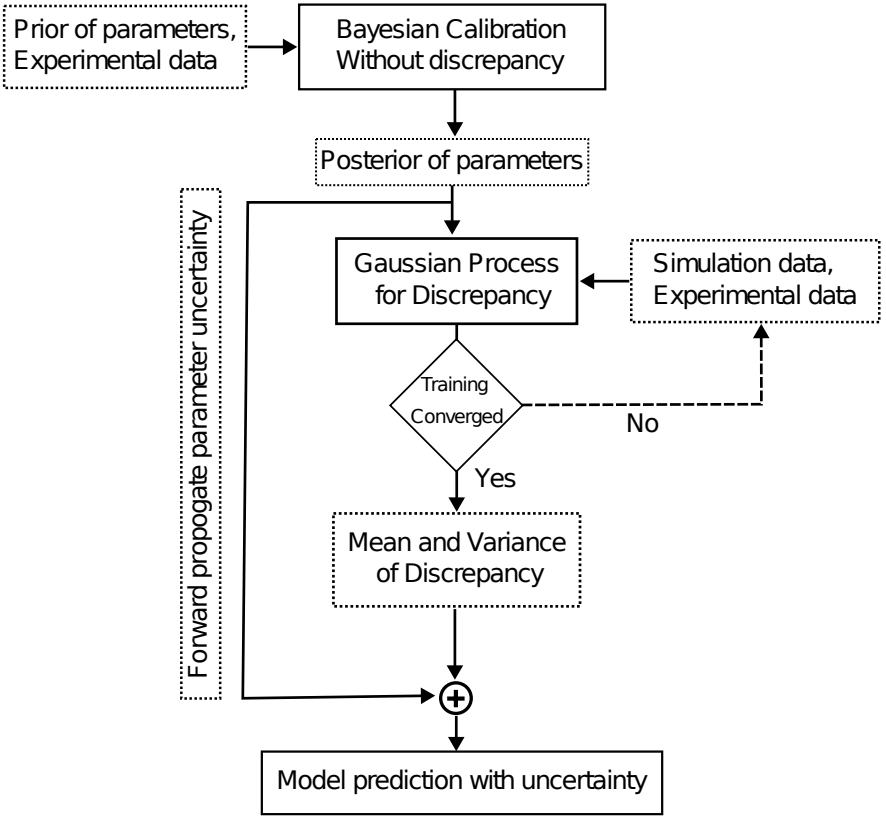
Figure 12: Uncertainty quantification framework

Bayesian calibration quantifies the parameter uncertainty and measurement errors, represented via the posterior distribution of the calibrated parameters. These uncertainties can be propagated through the computational model. The discrepancy function quantifies the uncertainties due to the modeling assumptions and/or missing physics. Hence, the total uncertainty in the prediction, $\boldsymbol{\Sigma}_{pred}(\boldsymbol{X})$, is the sum of the uncertainty in the computational

model, $\mathbf{\Sigma}_c(\boldsymbol{X}, \boldsymbol{\theta})$, and the uncertainty in the discrepancy function, $\mathbf{\Sigma}_\delta(\boldsymbol{X})$, and can be written as

$$\mathbf{\Sigma}_{pred}(\boldsymbol{X}) = \mathbf{\Sigma}_c(\boldsymbol{X}, \boldsymbol{\theta}) + \mathbf{\Sigma}_\delta(\boldsymbol{X}) \tag{41}$$

The uncertainty in the discrepancy function, $\mathbf{\Sigma}_\delta(\boldsymbol{X})$, is obtained from the GP model for the discrepancy. To quantify the modeling uncertainty, the uncertainties in the model's parameters are propagated through the CZM model by sampling the posterior distribution of parameters and evaluating the model at each of these samples [4]. The variance in the prediction of these samples, $\mathbf{\Sigma}_c(\boldsymbol{X}, \boldsymbol{\theta})$, is an estimate of the modeling uncertainty.

In a predictive setting, any new prediction $\boldsymbol{Y}_{pred}$ for the CZM can be evaluated as,

$$\boldsymbol{Y}_{pred} = Y_c(\boldsymbol{X}, \boldsymbol{\theta}^*) + \boldsymbol{\mu}_\delta \tag{42}$$

Where $Y_c(\boldsymbol{X}, \boldsymbol{\theta}^*)$ is the model's prediction at the calibrated parameters and $\boldsymbol{\mu}_\delta$ is the mean of the GP for discrepancy function. The diagonal values of $\mathbf{\Sigma}_{pred}$, denoted as $\boldsymbol{\sigma}^2_{pred}$ are used in determining the following confidence interval of predictions

$$\boldsymbol{Y}_{pred} \in \left[\boldsymbol{\mu}_{pred} - \Phi^{-1}\left(1 - \frac{\alpha}{2}\boldsymbol{\sigma}^2_{pred}\right), \; \boldsymbol{\mu}_{pred} + \Phi^{-1}\left(1 - \frac{\alpha}{2}\boldsymbol{\sigma}^2_{pred}\right) \right] \tag{43}$$

with probability $1 - \alpha$. Where $\Phi(.)$ is the cumulative distribution function of the Gaussian distribution.

4.4.1. Results of uncertainty quantification

Uncertainties are presented as 99.7% ($\pm 3\sigma$) confidence intervals in figure 13. These confidence intervals improve the reliability of the model's prediction. With the inclusion of the discrepancy function, all the experimental data lies well within the 99.7% confidence interval. The uncertainties are lower at the training points, i.e. points from the experiments used for calibration and for learning the discrepancy function, than at other points in the load-displacement curve.

---

[4]In this work, 1e5 samples from the posterior distribution of parameters are used to evaluate the uncertainty in the computational model.
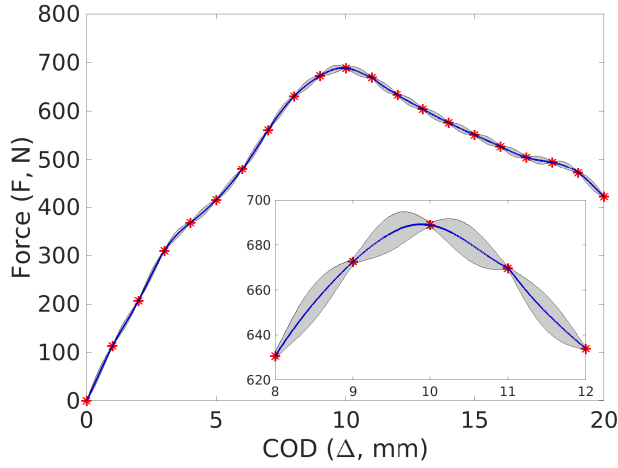
(a) 5 mm/min strain rate
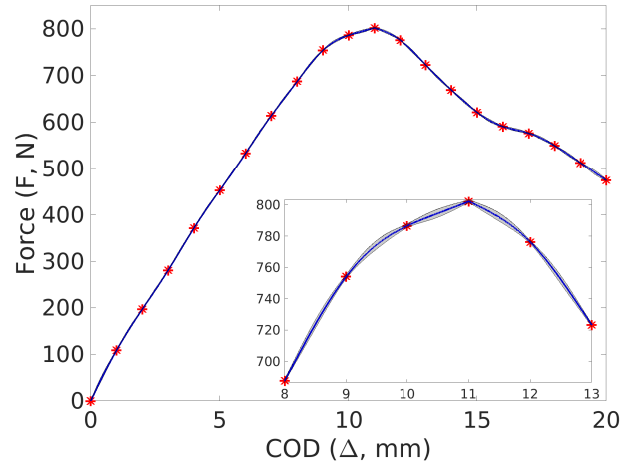
(b) 50 mm/min strain rate
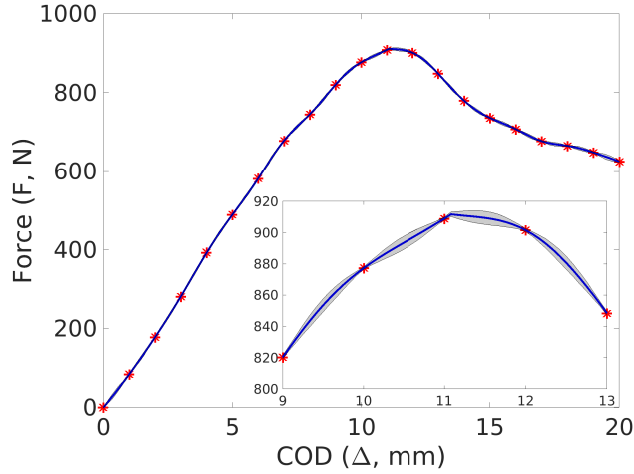
(c) 500 mm/min strain rate

Figure 13: Load–displacement curves predicted by the model along with the $\pm 3\sigma$ confidence intervals.

We observe that the contribution of the parameter uncertainty to the total uncertainty is less as compared to the contribution of the discrepancy function in Figure D.22, which is due to the following two reasons. First, the posterior distributions of the unknown parameters obtained through Bayesian calibration have small variance in most cases as seen from the density plots of the parameters in Figures 6, B.16 and B.16. Second, the GP model learned for the discrepancy function is purely data-driven and hence has high uncertainties where training data is unavailable, as seen in Figure 9. We also note that the uncertainty for the 5

mm/min strain rate (see the inset of Figure 13 (a)) is higher than the other two strain rates (see the inset of Figure 13 (b, c)). This could be attributed to the higher variation in the experimental data before the peak for the 5mm/min strain rate. For example in the small strain regime, the load-displacement curves of the 50 mm/min and the 500 mm/min strain rates are almost linear whereas the 5mm/min shows significant non-linearity.

5. Sensitivity Analysis

A sensitivity analysis provides a better understanding of the input-output relationship in the computational model. The contribution of individual input parameters to the output of the computational model can be studied from a sensitivity analysis. This also helps in the simplification of a model by treating the less sensitive random parameters as deterministic parameters.

A number of methods have been developed to perform sensitivity analysis in the literature [85]. These methods can be broadly classified as 1) local methods: which involve the study of small input perturbations around nominal values on the model output 2) global methods: which consider the range of the whole input domain. One such global method for sensitivity analysis is the Sobol' indices or the analysis of variance [86].

In this method, the total variance of a model is decomposed into the variance of the summands as,

$$\mathrm{Var}(Y) = \sum_{i=1}^{d} V_i + \sum_{i<j}^{d} V_{ij} + ... + V_{12...d}$$

where,

$$V_i = \mathrm{Var}_{X_i}[\mathbb{E}_{X_{\sim i}}(Y|X_i)]; \qquad V_{ij} = \mathrm{Var}_{X_{ij}}[\mathbb{E}_{X_{\sim ij}}(Y|X_{ij})] - V_i - V_j$$

and so on. The notation $X_{\sim i}$ indicates the set of all variables except X_i and $\mathbb{E}$ is the expectation.

The first-order indices are given by,

$$S_i = \frac{V_i}{\mathrm{Var}(Y)}$$

and the total-order indices are given by,

$$S_{Ti} = \frac{\mathbb{E}_{X_{\sim i}}[\mathrm{Var}_{X_i}(Y|X_i)]}{\mathrm{Var}(Y)}$$

5.1. Results of the sensitivity analysis

A sensitivity analysis is performed to assess the contribution of the parameters to the variance of the peak load predicted by the CZM. The parameters are sampled from the prior distributions to perform the sensitivity analysis. The Sobol' indices obtained by the sensitivity analysis are shown in Figure. 14. The displacement value at damage onset (δ^o) is the most sensitive parameter in determining the peak load. In classical damage mechanics analysis, the peak load/strength is governed by the damage initiation criterion. Likewise, in this work, we have the displacement at which the interface starts separating which is most sensitive to the peak load. The least sensitive parameters such as the reference plastic strain γ_o, Normal yield strength S_o, and the Hardening modulus H can be considered deterministic parameters thereby reducing the dimension of unknown parameters significantly.

(a) First order Sobol' indices   (b) Total Sobol' indices
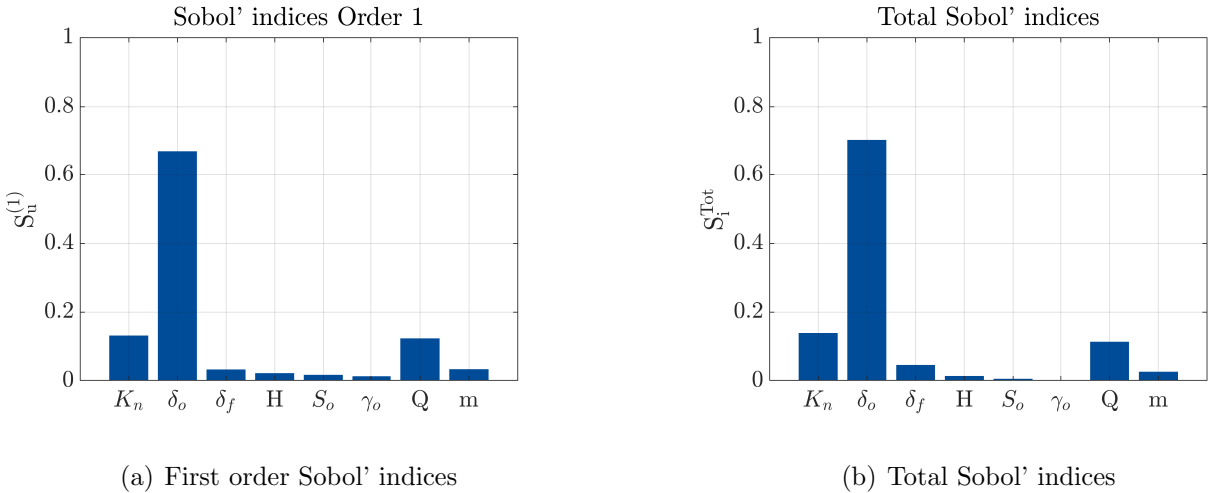
Figure 14: Sobol indices for the calibration parameters

5.2. Calibration for a subset of most sensitive parameters

In this subsection, the four least sensitive parameters, namely reference plastic strain γ_o, Normal yield strength S_o, Hardening modulus H, and Rate sensitivity parameter m, are con-

sidered deterministic thereby reducing the number of parameters that need to be calibrated by half. A Bayesian calibration is performed considering deterministic values of the above-mentioned parameters as the mean of their prior distributions. The mean and standard deviation of the posterior distributions of the four calibrated parameters obtained through this method are shown in the table. 5. The load-displacement curves obtained for the cali-

Parameter	Posterior	
	Mean	Std
Normal stiffness, K_N (MPa/mm)	570.6	1.4816
Displacement at the onset of damage, δ^0 (mm)	4.75	4.8e-3
Displacement at final failure, δ^f (mm)	13.21	3.8e-3
Activation energy, Q (N-mm)	2.24e-19	5.4e-22

Table 5: Mean and standard deviations of the Gaussian posteriors of Bayesian calibration

brated parameters are shown in Figure 15 . This figure demonstrates that the top 50% most sensitive parameters can capture the overall trend of the experimental load-displacement curves. However, the top 50% most sensitive parameters are not accurate enough to capture the experimental response compared to using all parameters. The reduction in performance is apparent in the post-peak response. Table 6 compares the errors between the CZM predictions and the experimental results when calibrating all parameters versus calibrating only the four most sensitive parameters. The higher errors might be attributed to the following factors: 1) The sensitivity analysis is performed using the prior of the parameters. The sensitivity of these parameters to the outputs may change significantly as we go farther away from the priors. Further, it is often challenging to obtain good prior distributions for the parameters, as in the case of this work, which might affect the results of sensitivity analysis. 2) The sensitivity analysis is performed on the peak load and not the entire load-displacement curve. Therefore, parameters that are insensitive to the peak load might still affect the model's performance in other regions of the load-displacement curve, such as the post-peak

response, resulting in an overall less accurate prediction. Nevertheless, in cases where the parameter space is too large to calibrate the entire set due to computational constraints, a sensitivity analysis can help perform a Bayesian calibration on a subset of the most sensitive parameters, significantly reducing the computational cost.
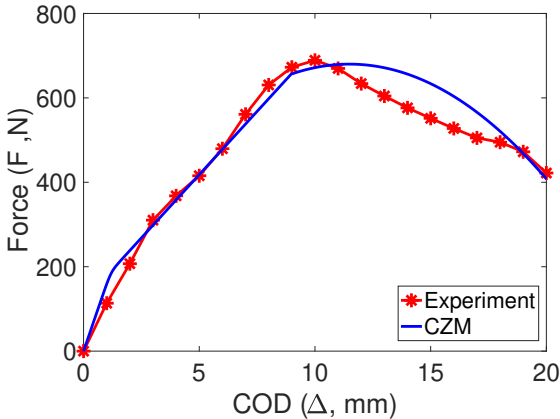
(a) 5 mm/min strain rate
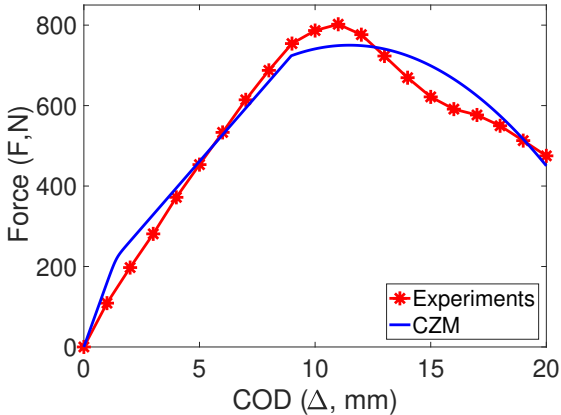
(b) 50 mm/min strain rate
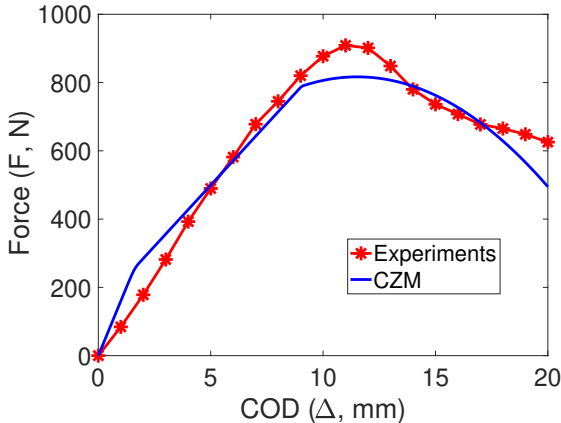
(c) 500 mm/min strain rate

Figure 15: Comparison of the load-displacement curves predicted by the CZM with the reduced parameter space obtained from sensitivity analysis.

Strain rate	% Error CZM (All parameters)	% Error CZM (4 parameters)
5 mm/min	5.10	8.13
50 mm/min	2.98	7.28
500 mm/min	3.20	8.66

Table 6: Percentage error in the CZM predictions with and without the discrepancy function

6. Conclusions

In the present work, a rate-dependent cohesive zone model (CZM) for the fracture of polymeric interfaces is presented. Calibrating numerous parameters for computational models, like the rate-dependent CZM, poses a challenge. Trial-and-error or nonlinear optimization methods frequently encounter issues of non-unique and inaccurate calibration. To overcome these challenges, we have implemented a Bayesian calibration approach, resulting in significantly improved accuracy of the CZM model. The Bayesian framework results in probability distributions for unknown parameters rather than a deterministic value. The variance of the probability distributions provides confidence intervals in the calibrated values and it serves as a tool to determine if additional experimental data is needed to enhance the accuracy of the calibration. In addition, these variances which are a measure of uncertainties in the parameter estimation have been propagated through the computational models to obtain uncertainties in the model prediction. A discrepancy function is learned to account for the average deviation between the model's predictions and experimental observations, effectively capturing modeling deficiencies. The model's predictive capability significantly improved through the utilization of the discrepancy function. Total uncertainties are quantified, and predictions are accompanied by confidence intervals. A sensitivity analysis is performed to generate insight into the input-output relationship for the model, identifying a small subset of parameters with the greatest influence. The techniques and the framework presented in this work are general and can be applied to any complex computational to perform calibration and uncertainty quantification.

Acknowledgments

References

[1] P. P. Camanho, C. G. Davila, M. F. de Moura, Numerical simulation of mixed-mode progressive delamination in composite materials, Journal of Composite Materials 37 (16) (2003) 1415–1438.

[2] F. Barpi, S. Valente, The cohesive frictional crack model applied to the analysis of the dam-foundation joint, Engineering Fracture Mechanics 77 (11) (2010) 2182–2191.

[3] N. Lu, Z. Suo, J. J. Vlassak, The effect of film thickness on the failure strain of polymer-supported metal films, Acta Materialia 58 (5) (2010) 1679 – 1687.

[4] C. Popelar, M. Kanninen, A dynamic viscoelastic analysis of crack propagation and crack arrest in a double cantilever beam test specimen, in: Crack Arrest Methodology and Applications, ASTM International, 1980.

[5] C. Xu, T. Siegmund, K. Ramani, Rate-dependent crack growth in adhesives II. experiments and analysis, International Journal of Adhesion and Adhesives 23 (1) (2003) 15 – 22.

[6] J. Du, M. Thouless, A. Yee, Effects of rate on crack growth in a rubber-modified epoxy, Acta materialia 48 (13) (2000) 3581–3592.

[7] C. Sun, M. Thouless, A. Waas, J. Schroeder, P. Zavattieri, Rate effects for mixed-mode fracture of plastically-deforming, adhesively-bonded structures, International Journal of Adhesion and Adhesives 29 (4) (2009) 434 – 443.

[8] A. Smiley, R. Pipes, Rate effects on mode I interlaminar fracture toughness in composite materials, Journal of composite materials 21 (7) (1987) 670–687.

[9] A. Smiley, R. Pipes, Rate sensitivity of mode II interlaminar fracture toughness in graphiteepoxy and graphite/peek composite materials, Composites science and technology 29 (1) (1987) 1–15.

[10] T. Kusaka, M. Hojo, Y.-W. Mai, T. Kurokawa, T. Nojima, S. Ochiai, Rate dependence of mode I fracture behaviour in carbon-fibreepoxy composite laminates, Composites Science and Technology 58 (3-4) (1998) 591–602.

[11] C.-Y. Hui, D.-B. Xu, E. J. Kramer, A fracture model for a weak interface in a viscoelastic material (small scale yielding analysis), Journal of applied physics 72 (8) (1992) 3294–3304.

[12] K. M. Liechti, J.-D. Wu, Mixed-mode, time-dependent rubber/metal debonding, Journal of the Mechanics and Physics of Solids 49 (5) (2001) 1039–1072.

[13] G. Giambanco, G. Fileccia Scimemi, Mixed mode failure analysis of bonded joints with rate-dependent interface models, International journal for numerical methods in engineering 67 (8) (2006) 1160–1192.

[14] S. Marzi, O. Hesebeck, M. Brede, F. Kleiner, A rate-dependent cohesive zone model for adhesively bonded joints loaded in mode i, Journal of adhesion science and technology 23 (6) (2009) 881–898.

[15] W. Knauss, G. Losi, Crack propagation in a nonlinearly viscoelastic solid with relevance to adhesive bond failure (1993).

[16] D. P. Makhecha, R. K. Kapania, E. R. Johnson, D. A. Dillard, G. C. Jacob, J. M. Starbuck, Rate-dependent cohesive zone modeling of unstable crack growth in an epoxy adhesive, Mechanics of Advanced Materials and Structures 16 (1) (2009) 12–19.

[17] T. Rabczuk, G. Zi, S. Bordas, H. Nguyen-Xuan, A simple and robust three-dimensional cracking-particle method without enrichment, Computer Methods in Applied Mechanics and Engineering 199 (37-40) (2010) 2437–2455.

[18] C. M. Landis, T. Pardoen, J. W. Hutchinson, Crack velocity dependent toughness in rate dependent materials, Mechanics of materials 32 (11) (2000) 663–678.

[19] I. Mohammed, M. Charalambides, A. Kinloch, Modeling the effect of rate and geometry on peeling and tack of pressure-sensitive adhesives, Journal of Non-Newtonian Fluid Mechanics 233 (2016) 85–94.

[20] M. Elices, G. Guinea, J. Gomez, J. Planas, The cohesive zone model: advantages, limitations and challenges, Engineering fracture mechanics 69 (2) (2002) 137–163.

[21] A. Ghatak, K. Vorvolakos, H. She, D. L. Malotky, M. K. Chaudhury, Interfacial rate processes in adhesion and friction (2000).

[22] P. Rahul-Kumar, A. Jagota, S. Bennison, S. Saigal, S. Muralidhar, Polymer interfacial fracture simulations using cohesive elements, Acta materialia 47 (15-16) (1999) 4161–4169.

[23] D. E. Spearot, K. I. Jacob, D. L. McDowell, Non-local separation constitutive laws for interfaces and their relation to nanoscale simulations, Mechanics of Materials 36 (9) (2004) 825–847.

[24] A. Needleman, An analysis of decohesion along an imperfect interface, in: Non-Linear Fracture, Springer, 1990, pp. 21–40.

[25] V. Tvergaard, J. W. Hutchinson, The relation between crack growth resistance and fracture process parameters in elastic-plastic solids, Journal of the Mechanics and Physics of Solids 40 (6) (1992) 1377–1397.

[26] X.-P. Xu, A. Needleman, Numerical simulations of fast crack growth in brittle solids, Journal of the Mechanics and Physics of Solids 42 (9) (1994) 1397–1434.

[27] G. T. Camacho, M. Ortiz, Computational modelling of impact damage in brittle materials, International Journal of solids and structures 33 (20-22) (1996) 2899–2938.

[28] Q. Yang, M. Thouless, S. Ward, Numerical simulations of adhesively-bonded beams failing with extensive plastic deformation, Journal of the Mechanics and Physics of Solids 47 (6) (1999) 1337–1353.

[29] Y. Gao, A. Bower, A simple technique for avoiding convergence problems in finite element simulations of crack nucleation and growth on cohesive interfaces, Modelling and Simulation in Materials Science and Engineering 12 (3) (2004) 453.

[30] Y. Wei, H. Gao, A. F. Bower, Numerical simulations of crack deflection at a twist-misoriented grain boundary between two ideally brittle crystals, Journal of the Mechanics and Physics of Solids 57 (11) (2009) 1865–1879.

[31] Y. Wei, Entropic-elasticity-controlled dissociation and energetic-elasticity-controlled rupture induce catch-to-slip bonds in cell-adhesion molecules, Physical Review E 77 (3) (2008) 031910.

[32] C. Su, Y. Wei, L. Anand, An elastic–plastic interface constitutive model: application to adhesive joints, International Journal of Plasticity 20 (12) (2004) 2063 – 2081.

[33] Y. Wei, A. F. Bower, H. Gao, Analytical model and molecular dynamics simulations of the size dependence of flow stress in amorphous intermetallic nanowires at temperatures near the glass transition, Physical Review B 81 (12) (2010) 125402.

[34] C. Xu, T. Siegmund, K. Ramani, Rate-dependent crack growth in adhesives: I. modeling approach, International Journal of Adhesion and Adhesives 23 (1) (2003) 9 – 13.

[35] A. Corigliano, M. Ricci, Rate-dependent interface models: formulation and numerical applications, International Journal of Solids and Structures 38 (4) (2001) 547 – 576.

[36] A. Corigliano, S. Mariani, A. Pandolfi, Numerical modeling of rate-dependent debonding processes in composites, Composite Structures 61 (1-2) (2003) 39–50.

[37] M. Anvari, I. Scheider, C. Thaulow, Simulation of dynamic ductile crack growth using strain-rate and triaxiality-dependent cohesive elements, Engineering fracture mechanics 73 (15) (2006) 2210–2228.

[38] A. Rosa, R. Yu, G. Ruiz, L. Saucedo, J. Sousa, A loading rate dependent cohesive model for concrete fracture, Engineering Fracture Mechanics 82 (2012) 195–208.

[39] M. May, O. Hesebeck, S. Marzi, W. Böhme, J. Lienhard, S. Kilchert, M. Brede, S. Hiermaier, Rate dependent behavior of crash-optimized adhesives–experimental characterization, model development, and simulation, Engineering Fracture Mechanics 133 (2015) 112–137.

[40] A. Corigliano, S. Mariani, A. Pandolfi, Numerical analysis of rate-dependent dynamic composite delamination, Composites Science and Technology 66 (6) (2006) 766–775.

[41] M. Musto, G. Alfano, A novel rate-dependent cohesive-zone model combining damage and visco-elasticity, Computers & Structures 118 (2013) 126 – 133, special Issue: UK Association for Computational Mechanics in Engineering.

[42] M. Musto, G. Alfano, A fractional rate-dependent cohesive-zone model, International Journal for Numerical Methods in Engineering 103 (5) (2015) 313–341, nme.4885.

[43] O. Giraldo-Londoño, D. W. Spring, G. H. Paulino, W. G. Buttlar, An efficient mixed-mode rate-dependent cohesive fracture model using sigmoidal functions, Engineering Fracture Mechanics (2017).

[44] Z. Lu, Q. Xu, Cohesive zone modeling for viscoplastic behavior at finite deformations, Composites Science and Technology 74 (2013) 173 – 178.

[45] S. Dey, T. Mukhopadhyay, H. H. Khodaparast, S. Adhikari, Fuzzy uncertainty propagation in composites using gram–schmidt polynomial chaos expansion, Applied Mathematical Modelling 40 (7-8) (2016) 4412–4428.

[46] G. Stevens, S. Atamturktur, R. Lebensohn, G. Kaschner, Experiment-based validation and uncertainty quantification of coupled multi-scale plasticity models, Multidiscipline Modeling in Materials and Structures (2016).

[47] D. E. Ricciardi, O. A. Chkrebtii, S. R. Niezgoda, Uncertainty quantification accounting for model discrepancy within a random effects bayesian framework, Integrating Materials and Manufacturing Innovation (2020) 1–18.

[48] P. Miles, M. Hays, R. Smith, W. Oates, Bayesian uncertainty analysis of finite deformation viscoelasticity, Mechanics of Materials 91 (2015) 35–49.

[49] F. Liu, M. Bayarri, J. Berger, R. Paulo, J. Sacks, A bayesian analysis of the thermal challenge problem, Computer Methods in Applied Mechanics and Engineering 197 (29-32) (2008) 2457–2466.

[50] D. Higdon, C. Nakhleh, J. Gattiker, B. Williams, A bayesian calibration approach to the thermal problem, Computer Methods in Applied Mechanics and Engineering 197 (29-32) (2008) 2431–2441.

[51] M. C. Kennedy, A. O'Hagan, Bayesian calibration of computer models, Journal of the Royal Statistical Society: Series B (Statistical Methodology) 63 (3) (2001) 425–464.

[52] D. Higdon, M. Kennedy, J. C. Cavendish, J. A. Cafeo, R. D. Ryne, Combining field data and computer simulations for calibration and prediction, SIAM Journal on Scientific Computing 26 (2) (2004) 448–466.

[53] D. Higdon, J. Gattiker, B. Williams, M. Rightley, Computer model calibration using high-dimensional output, Journal of the American Statistical Association 103 (482) (2008) 570–583.

[54] P. Z. Qian, C. J. Wu, Bayesian hierarchical modeling for integrating low-accuracy and high-accuracy experiments, Technometrics 50 (2) (2008) 192–204.

[55] P. D. Arendt, D. W. Apley, W. Chen, Quantification of model uncertainty: Calibration, model discrepancy, and identifiability, Journal of Mechanical Design 134 (10) (2012).

[56] P. D. Arendt, D. W. Apley, W. Chen, D. Lamb, D. Gorsich, Improving identifiability in model calibration using multiple responses, Journal of Mechanical Design 134 (10) (2012).

[57] K. A. Maupin, L. P. Swiler, Model discrepancy calibration across experimental settings, Reliability Engineering & System Safety (2020) 106818.

[58] M. Goldstein, J. Rougier, Reified bayesian modelling and inference for physical systems, Journal of statistical planning and inference 139 (3) (2009) 1221–1239.

[59] M. J. Bayarri, J. O. Berger, R. Paulo, J. Sacks, J. A. Cafeo, J. Cavendish, C.-H. Lin, J. Tu, A framework for validation of computer models, Technometrics 49 (2) (2007) 138–154.

[60] R. B. Gramacy, H. K. H. Lee, Bayesian treed gaussian process models with an application to computer modeling, Journal of the American Statistical Association 103 (483) (2008) 1119–1130.

[61] Y. Ling, J. Mullins, S. Mahadevan, Selection of model discrepancy priors in bayesian calibration, Journal of Computational Physics 276 (2014) 665–680.

[62] E. Asaadi, P. S. Heyns, A computational framework for bayesian inference in plasticity models characterisation, Computer Methods in Applied Mechanics and Engineering 321 (2017) 455–481.

[63] W. N. Edeling, P. Cinnella, R. P. Dwight, H. Bijl, Bayesian estimates of parameter variability in the k–ε turbulence model, Journal of Computational Physics 258 (2014) 73–94.

[64] M. Ortiz, A. Pandolfi, Finite-deformation irreversible cohesive elements for three-dimensional crack-propagation analysis, International journal for numerical methods in engineering 44 (9) (1999) 1267–1282.

[65] Q. Xu, Z. Lu, An elastic–plastic cohesive zone model for metal–ceramic interfaces at finite deformations, International Journal of Plasticity 41 (2013) 147–164.

[66] J. Richeton, S. Ahzi, L. Daridon, Y. Rémond, A formulation of the cooperative model for the yield stress of amorphous polymers for a wide range of strain rates and temperatures, Polymer 46 (16) (2005) 6035–6043.

[67] J. Richeton, S. Ahzi, K. Vecchio, F. Jiang, R. Adharapurapu, Influence of temperature and strain rate on the mechanical behavior of three amorphous polymers: characterization and modeling of the compressive yield stress, International journal of solids and structures 43 (7-8) (2006) 2318–2335.

[68] L. Anand, N. M. Ames, V. Srivastava, S. A. Chester, A thermo-mechanically coupled theory for large deformations of amorphous polymers. part i: Formulation, International Journal of Plasticity 25 (8) (2009) 1474–1494.

[69] N. M. Ames, V. Srivastava, S. A. Chester, L. Anand, A thermo-mechanically coupled theory for large deformations of amorphous polymers. part ii: Applications, International Journal of Plasticity 25 (8) (2009) 1495–1539.

[70] H. Eyring, Viscosity, plasticity, and diffusion as examples of absolute reaction rates, The Journal of chemical physics 4 (4) (1936) 283–291.

[71] A. Argon, A theory for the low-temperature plastic deformation of glassy polymers, Philosophical Magazine 28 (4) (1973) 839–865.

[72] A. Mulliken, M. Boyce, Mechanics of the rate-dependent elastic–plastic deformation of glassy polymers from low to high strain rates, International journal of solids and structures 43 (5) (2006) 1331–1356.

[73] D. Fotheringham, B. Cherry, The role of recovery forces in the deformation of linear polyethylene, Journal of materials science 13 (5) (1978) 951–964.

[74] D. Fotheringham, B. Cherry, C. Bauwens-Crowet, Comment on "the compression yield behaviour of polymethyl methacrylate over a wide range of temperatures and strain-rates", Journal of Materials Science 11 (7) (1976) 1368–1371.

[75] K. Pandya, J. Williams, Measurement of cohesive zone parameters in tough polyethylene, Polymer Engineering & Science 40 (8) (2000) 1765–1776.

[76] V. Srivastava, S. A. Chester, N. M. Ames, L. Anand, A thermo-mechanically-coupled large-deformation theory for amorphous polymers in a temperature range which spans their glass transition, International Journal of Plasticity 26 (8) (2010) 1138–1182.

[77] Overview of materials for high density polyethylene (hdpe), extruded, `https://www.matweb.com/search/datasheet_print.aspx?matguid=482765fad3b443169ec28fb6f9606660`, accessed: 11-08-2023.

[78] C. M. Bishop, N. M. Nasrabadi, Pattern recognition and machine learning, Vol. 4, Springer, 2006.

[79] J. Kaipio, E. Somersalo, Statistical and computational inverse problems, Vol. 160, Springer Science & Business Media, 2006.

[80] E. Torre, S. Marelli, B. Sudret, UQLab user manual – Statistical inference, Tech. rep., Chair of Risk, Safety and Uncertainty Quantification, ETH Zurich, Switzerland, report: UQLab-V1.3-114 (2019).

[81] S. Marelli, B. Sudret, Uqlab: A framework for uncertainty quantification in matlab, in: Vulnerability, uncertainty, and risk: quantification, mitigation, and management, 2014, pp. 2554–2563.

[82] J. C. Lagarias, J. A. Reeds, M. H. Wright, P. E. Wright, Convergence properties of the nelder–mead simplex method in low dimensions, SIAM Journal on optimization 9 (1) (1998) 112–147.

[83] C. Rasmussen, C. Williams, Gaussian processes for machine learning, ser. adaptive computation and machine learning, Cambridge, MA, USA: MIT Press 38 (2006) 715–719.

[84] T. J. Santner, B. J. Williams, W. Notz, B. J. Williams, The design and analysis of computer experiments, Vol. 1, Springer, 2003.

[85] B. Iooss, P. Lemaître, A review on global sensitivity analysis methods, in: Uncertainty management in simulation-optimization of complex systems, Springer, 2015, pp. 101–122.

[86] I. M. Sobol, Sensitivity analysis for non-linear mathematical models, Mathematical modelling and computational experiment 1 (1993) 407–414.

[87] J. Goodman, J. Weare, Ensemble samplers with affine invariance, Communications in applied mathematics and computational science 5 (1) (2010) 65–80.

Appendix A. Affine invariant Ensemble algorithm

The affine invariant Ensemble (AIES) [87] algorithm is an MCMC method that can be used to sample from the posterior distribution of parameters. The primary advantage of the AIES algorithm is that it performs well when the posterior distribution shows a strong correlation between the parameters due to its property of being invariant to affine transformations of the target distribution [80]. In contrast, other MCMC algorithms perform poorly when the parameters are correlated and need a considerable amount of tuning to improve performance.

In the AIES algorithm, an ensemble of Markov chains $\chi_1, \chi_2, ...\chi_c$ called *walkers* is considered. The position of a chain θ_i is updated by randomly picking a conjugate chain $\theta_j^{(t)}$ such that $i \neq j$. As a next step, a *stretch move* is performed where a new position $\theta_i^{(*)}$ is proposed such that

$$\theta_i^{(*)} = \theta_i^{(t)} + Z(\theta_j^{(t)} - \theta_i^{(t)}) \tag{A.1}$$

where,

$$Z \sim p(z) = \begin{cases} \dfrac{1}{\sqrt{z}\left(2\sqrt{a} - \frac{2}{\sqrt{a}}\right)} & \text{if } z \in [1/a, a], \\ 0 & \text{otherwise.} \end{cases} \tag{A.2}$$

where $a > 1$ is a tuning parameter. $\theta_i^{(*)}$ is then accepted as the new position of the i-th walker with probability:

$$\alpha(\theta_i^{(*)}, \theta_i^{(t)}, z) = \min\left\{1, z^{M-1} \frac{\pi(\theta_i^{(*)}|\mathcal{D})}{\pi(\theta_i^{(t}|\mathcal{D})}\right\} \tag{A.3}$$

This is done for all the chains in the ensemble to obtain the samples from the posterior distribution of parameters.

Appendix B. Analysis of the posterior of parameters

In MCMC methods, trace plots serve as an important tool to diagnose the convergence of MCMC chains. Trace plots track the individual Markov chains during the optimization process. Trace plots for the 100 random initialized chains are presented in Figure. B.16. Note that the posterior distribution is obtained after burning out 50% of the initial samples, however all the samples are shown here for completeness. The plots for the parameters $K_N, \delta_o, \delta_f, H$ and γ_o show good convergence. Given that the calibration is performed in high (eight) dimensions the plots for the parameters S_o, Q, and m are reasonable.
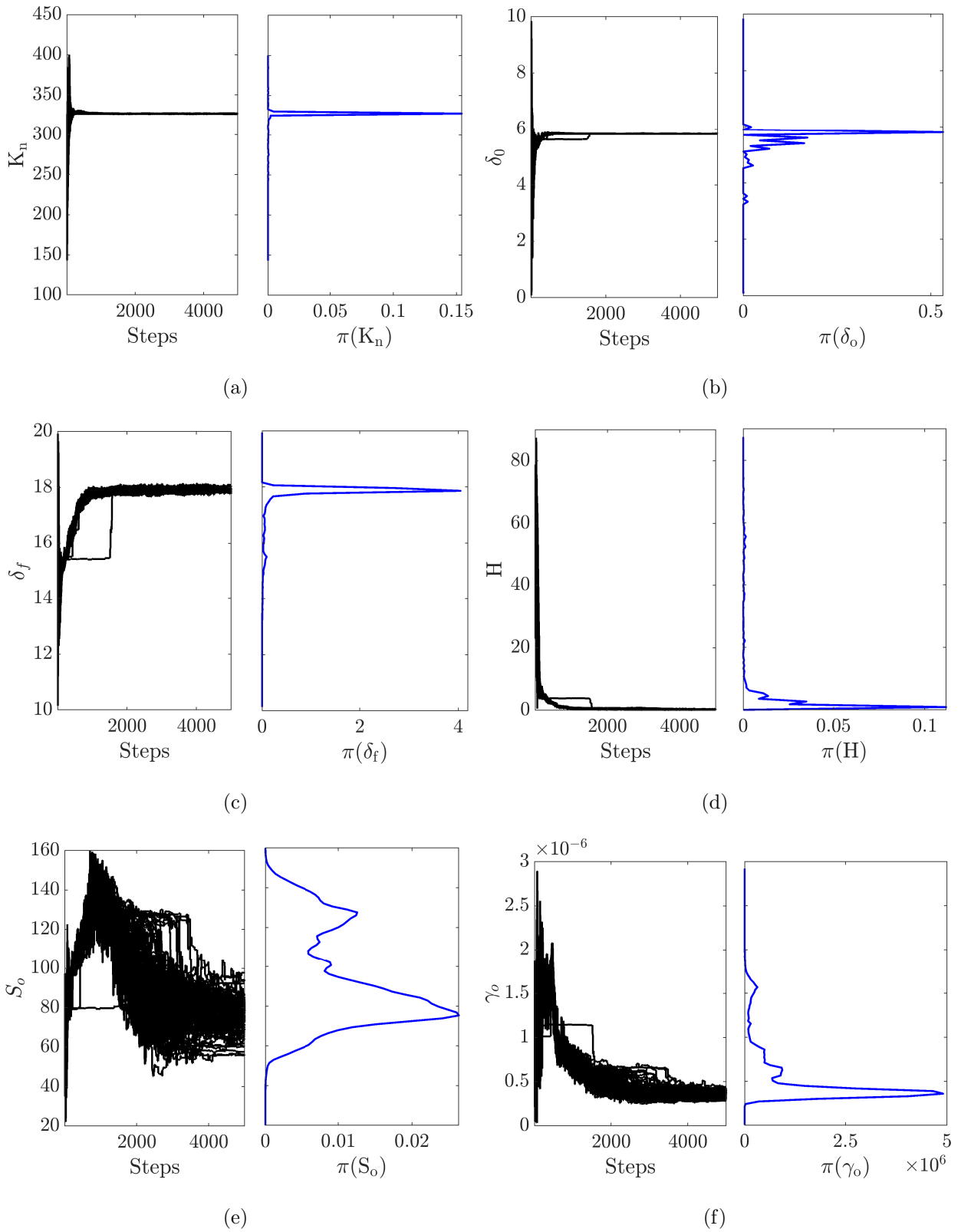
Figure B.16: Trace and density plots of the parameters
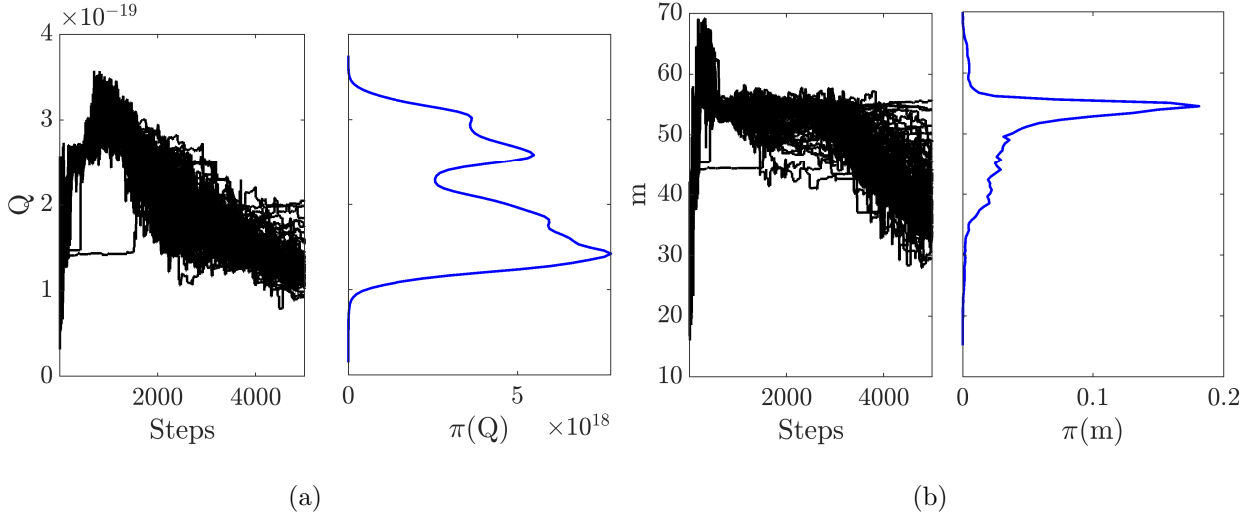
Figure B.16: Trace and density plots of the parameters

The convergence of the mean of the parameters is shown in Figure. B.17. The mean convergence plots show the same trend as the trace plots.
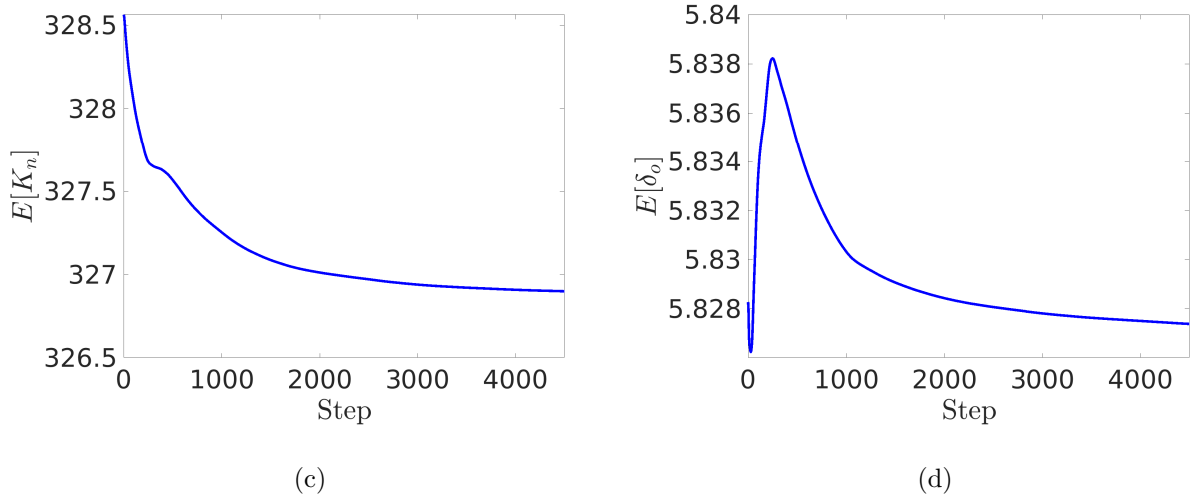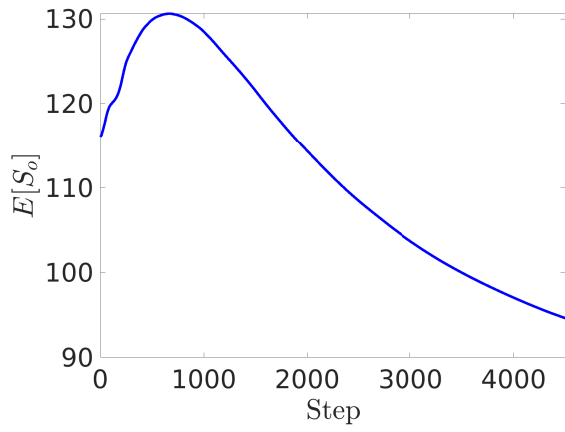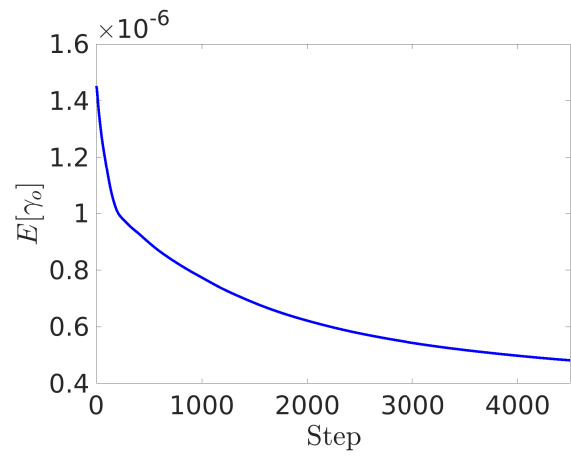

Figure B.17: Convergence of the means of the parameters
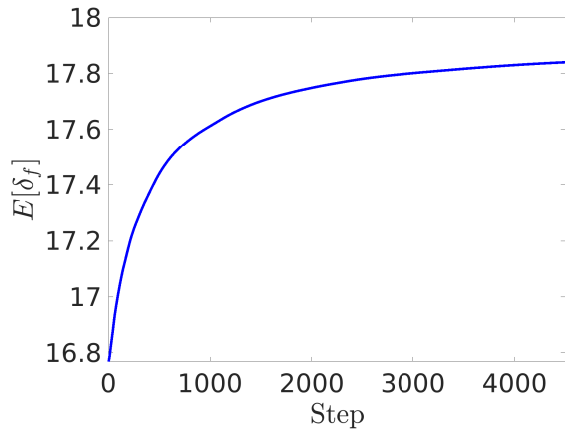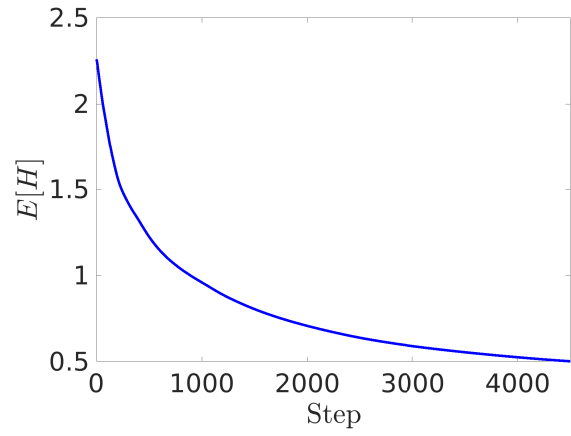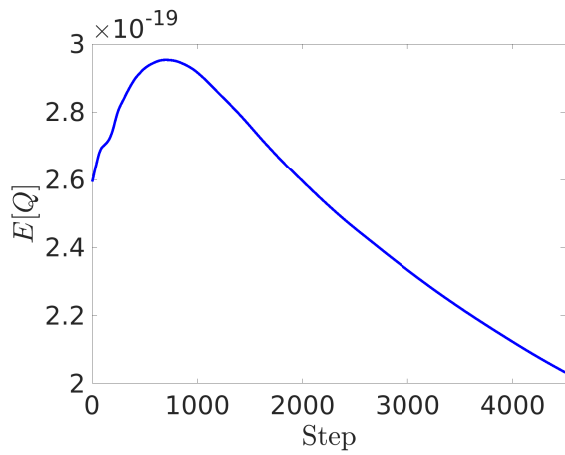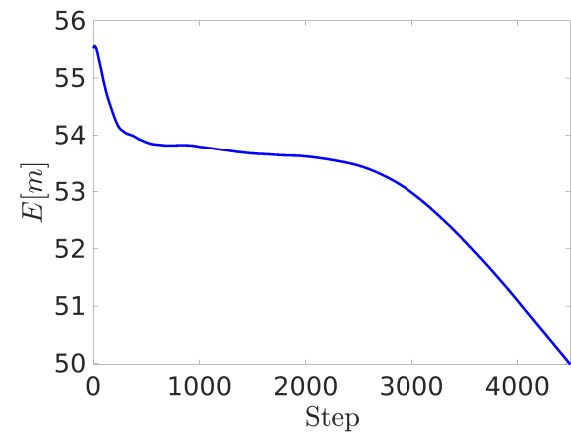
Figure B.17: Convergence of the means of the parameters

A violin plot is a statistical graph showing the probability density of a quantity. Violin plots depicting the posterior predictive distribution of the load-displacement curve are presented in Figure B.18. The effect of the parameter uncertainty is seen from the violin plots. It is evident that the parameter uncertainties are not sufficient to capture the experimental response. This emphasizes the need for a discrepancy term.
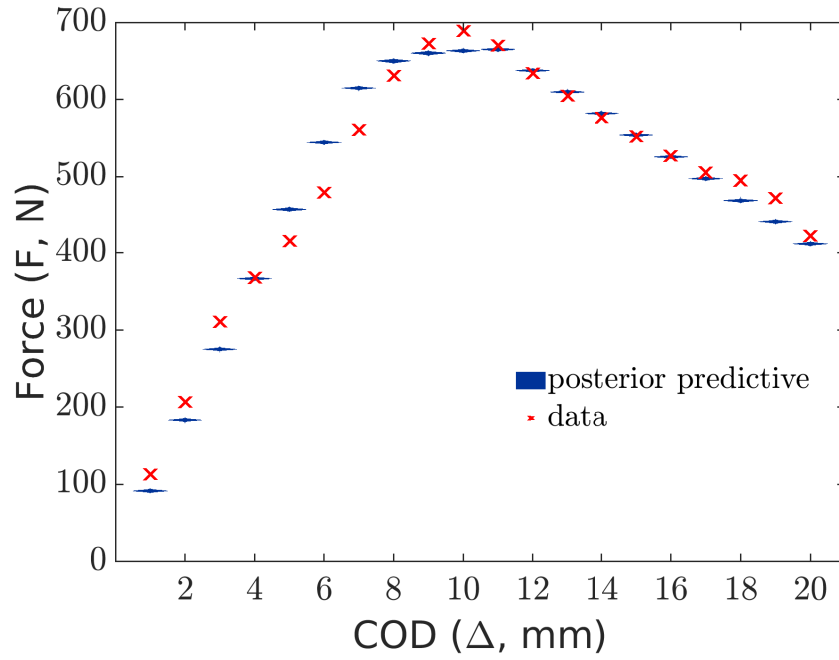
(g) 5 mm/min
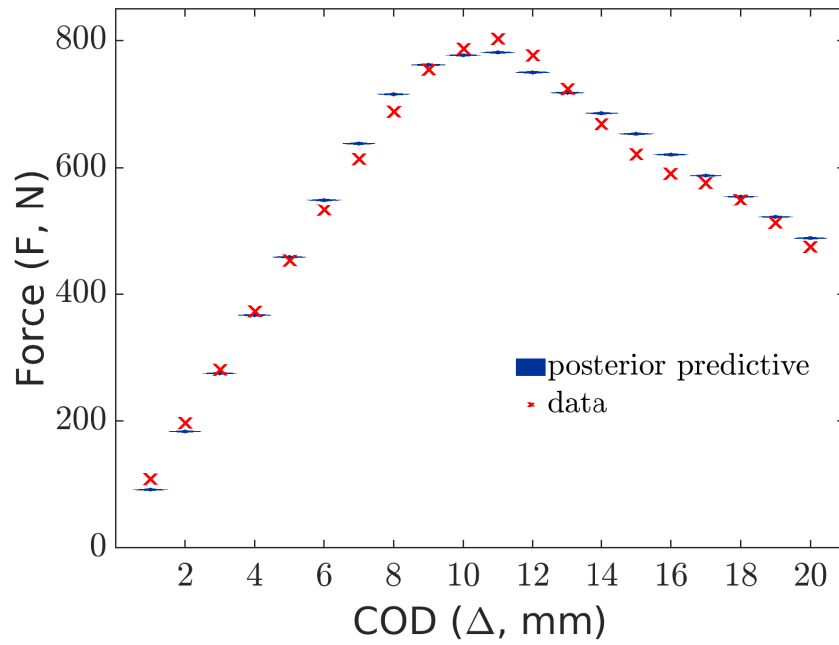
(h) 50 mm/min

Figure B.18: Posterior predictive distribution after Bayesian Calibration
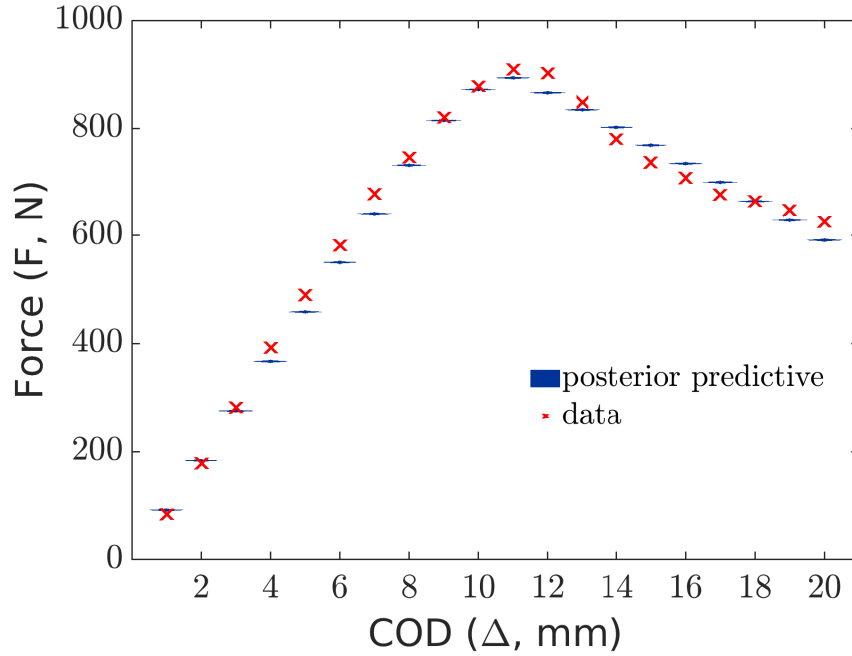
(a) 500 mm/min

Figure B.18: Posterior predictive distribution after Bayesian Calibration

The samples drawn from the prior and posterior distribution of parameters are presented through a scatterplot in Figure B.19 and B.20 respectively. Since the material parameters cannot be uniquely determined from limited experimental data, a stochastic approach such as the Bayesian calibration used in this work provides us with all possible values of the parameters, as seen in B.20, that can reproduce the experiments. The variance of these samples is a measure of uncertainty in the parameters of the model.

Appendix C. Error convergence study of the Gaussian process model

In this work, a Gaussian process (GP) model is used to learn the discrepancy between the computational model's output and the experimental response. A convergence study for the error between the GP's prediction and the true discrepancy is performed to select the optimal number of points needed to learn the discrepancy function. The plot of the convergence of

the percentage error is shown in Figure. C.21. Based on this study, 20 points are taken to learn the discrepancy function.
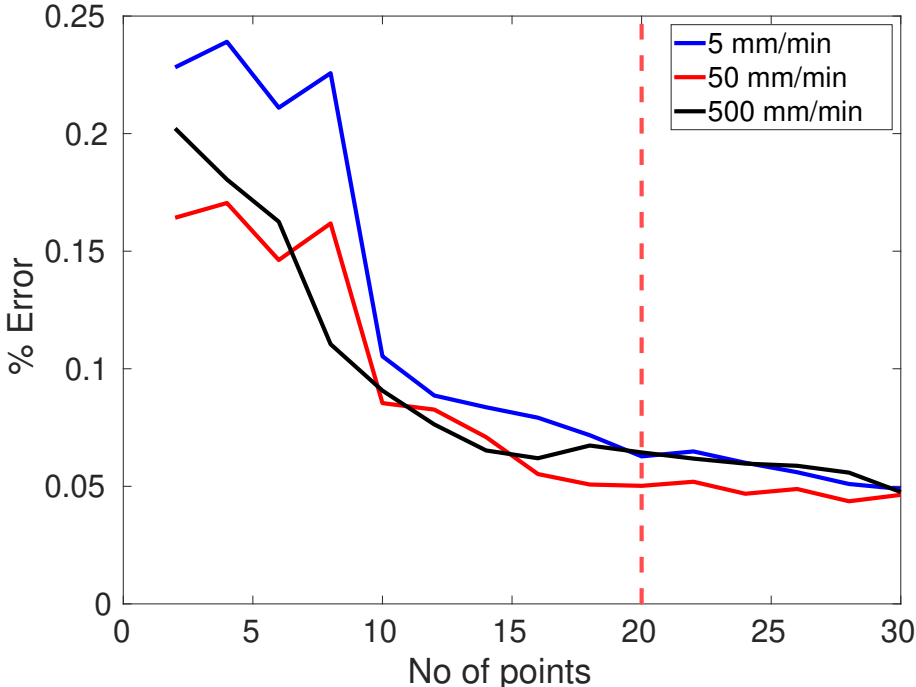

Figure C.21: Convergence of error with the number of training points in discrepancy.

Appendix D. Contribution to Uncertainties

We compare the contribution of the discrepancy and the parameter uncertainty to the overall uncertainty of the CZM in Figure D.22. A similar trend was observed for all three strain rates.
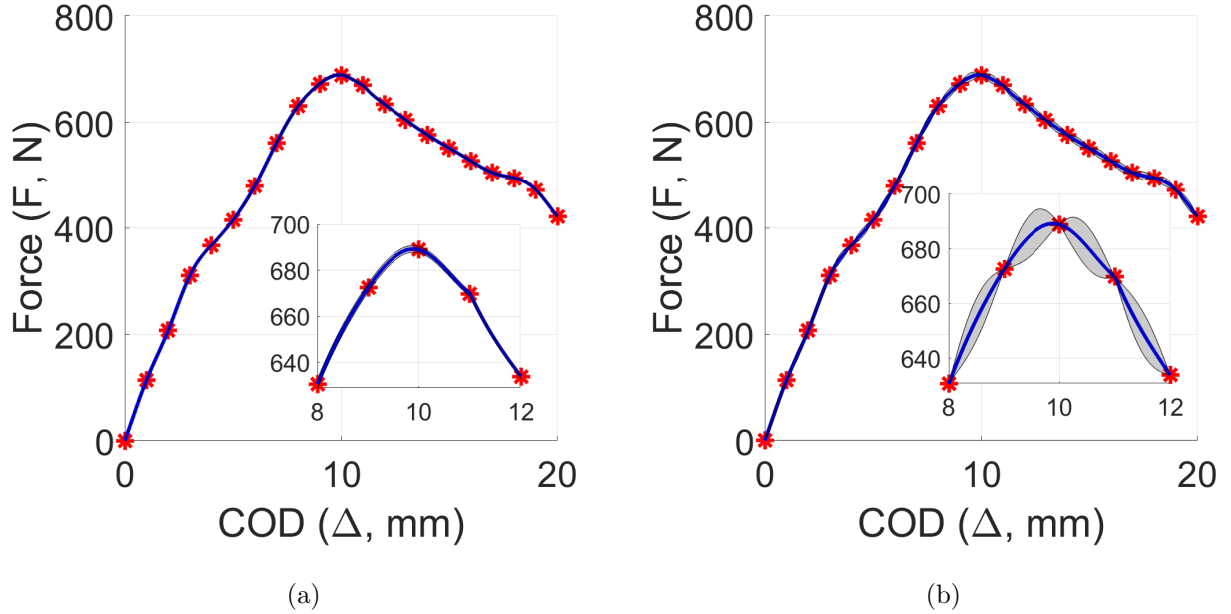
Figure D.22: Uncertainty due to: (a) calibration (parameter uncertainty) and (b) Gaussian process of the discrepancy function for the 5mm/min strain rate.

Appendix E. Energy release rates

In this section we compute the energy release rates based on the presented P-COD curves. We used the "Change in compliance approach" for this purpose, where compliance (C) for a DCB specimen is given by

$$C = \frac{u}{P} = 8\frac{a^3}{EBh^3} \tag{E.1}$$

Where, u is the COD, P is the load, a is the crack length, E is Young's modulus, B is the specimen width and h is the cantilever height. Therefore, the crack length (a) evolution can be evaluated using (E.1) and based on the load-displacement data. With the crack length known, we further obtain the energy release rate as,

$$G = \frac{12a^2P^2}{Eb^2h^3} \tag{E.2}$$

Figure. E.23 depicts the strain energy release rate (G) normalized by its value at crack initiation (G_{IC}) vs change in crack length (Δa). The increasing trend of G as a function of

61

crack length depicts a stable crack growth trend for the specimens. It is also to be noted that the compliance calibration method considers the beams to be deformable rather than rigid as assumed in the proposed rate-dependent cohesive model.
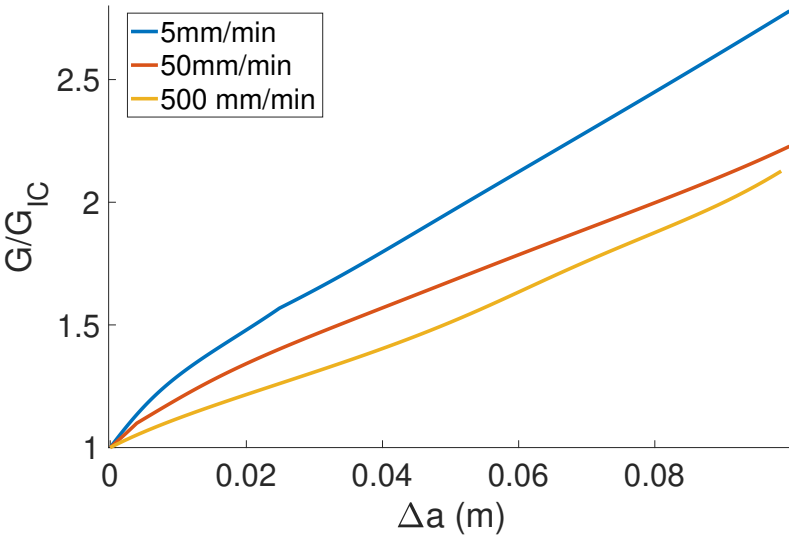
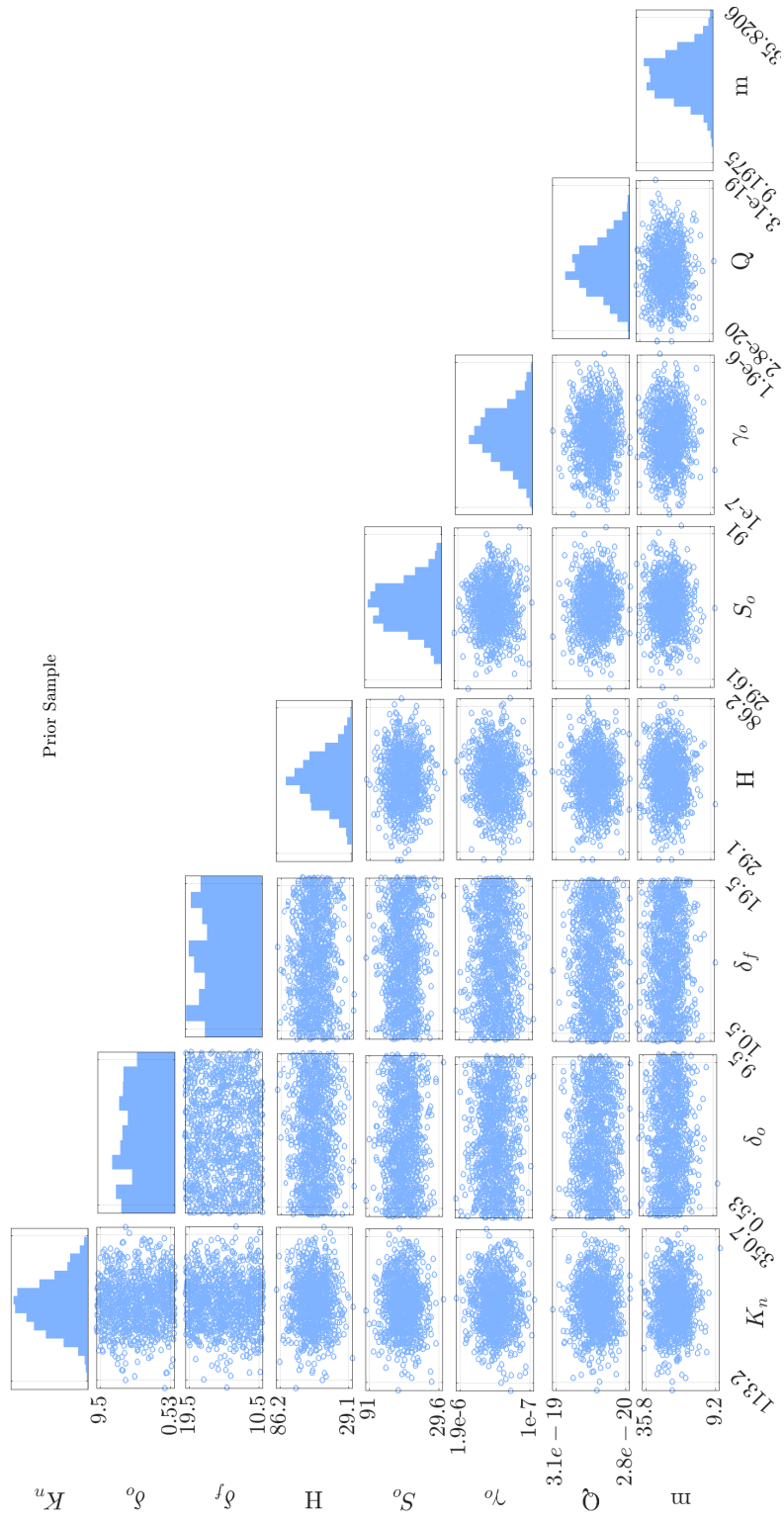

Figure E.23: Strain energy release rate

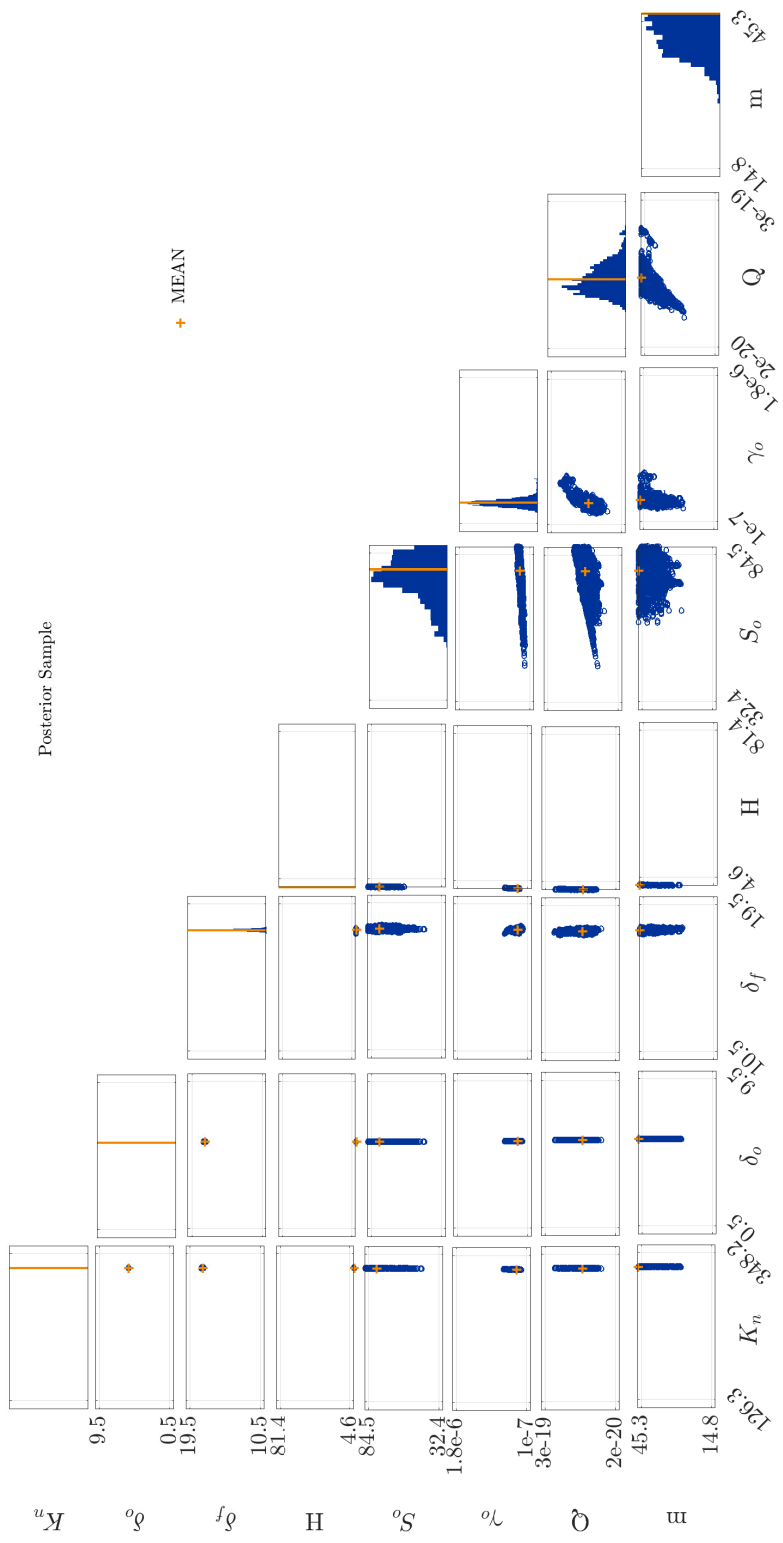Figure B.19: Samples drawn from prior distributions during calibration.

Figure B.20: Samples drawn from posterior distributions during calibration.